



# Rapid structural transformation of ionizable lipid nanoparticles involving Omega-3 polyunsaturated fatty acids enhances antioxidant defense and mitochondrial proteins activity in pH-responsive drug delivery

Thelma Akanchise<sup>a</sup>, Fucen Luo<sup>a</sup>, Borislav Angelov<sup>b,\*</sup>, Yuru Deng<sup>c,d</sup>, Gouranga Manna<sup>e</sup>, Angelina Angelova<sup>a,\*</sup>

<sup>a</sup> Université Paris-Saclay, CNRS, Institut Galien Paris-Saclay, 91400 Orsay, France

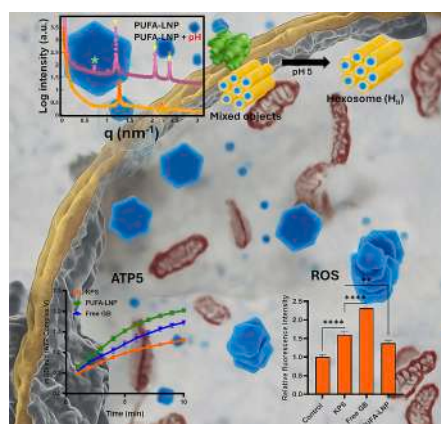
<sup>b</sup> Extreme Light Infrastructure ERIC, Department of Structural Dynamics, Za Radnici 835, 25241 Dolni Brezany, Czech Republic

<sup>c</sup> Wenzhou Institute, University of Chinese Academy of Sciences, Wenzhou, China

<sup>d</sup> Wenzhou Yuanpai Biotechnology Co., Ltd., Wenzhou, China

<sup>e</sup> ESRF, The European Synchrotron, 71 avenue des Martyrs, 38043, Grenoble, France

## GRAPHICAL ABSTRACT



## ARTICLE INFO

**Keywords:**  
Hexosomes  
Cubosomes

## ABSTRACT

Inefficient intracellular delivery remains a major bottleneck in the development of nanomedicines targeting brain disorders. To address this challenge, we present a dynamic structural nanomedicine platform based on ionizable liquid crystalline lipid nanoparticles (LC-LNPs) incorporating omega-3 polyunsaturated fatty acids

**Abbreviations:** ECT, Electron transport chain;  $\Delta\psi_m$ , Mitochondrial membrane potential changes; ROS, Reactive oxygen species; Cyt C, Cytochrome c; SOD, Superoxide dismutase; CAT, Catalase; GSH-Px, Glutathione peroxidase; TCA, Tricarboxylic acid cycle; ATP, Adenosine triphosphate; ADP, Adenosine diphosphate; PI3K, Phosphatidylinositol-3 kinase; Raf, Rapidly accelerated fibrosarcoma; PLCs, Phosphoinositide-specific phospholipase C; PKC, Protein kinase C;  $Ca^{2+}$ , Calcium ion; PDK1, Phosphoinositide-dependent kinase-1; AKT, Protein kinase B; MEK, Mitogen-activated protein kinase; ERK, Extracellular signal-regulated kinase; CREB, Cyclic AMP (cAMP)-response element-binding protein; BDNF, Brain-derived neurotrophic factor; KPS, potassium persulfate.

\* Corresponding authors.

E-mail address: [angelina.angelova@universite-paris-saclay.fr](mailto:angelina.angelova@universite-paris-saclay.fr) (A. Angelova).

<https://doi.org/10.1016/j.jcis.2025.139420>

Received 15 September 2025; Received in revised form 15 October 2025; Accepted 6 November 2025

Available online 7 November 2025

0021-9797/© 2025 The Authors. Published by Elsevier Inc. This is an open access article under the CC BY-NC license (<http://creativecommons.org/licenses/by-nc/4.0/>).

pH-induced structural transformations  
Time-resolved SAXS  
Nose-to-brain delivery  
PACAP  
PUFAs

(PUFAs), enabling pH-responsive transformation and neuroprotective drug delivery. The created multidrug-loaded nonlamellar LC-LNP co-encapsulated the antioxidants ginkgolide B and quercetin and were functionalized with the bioactive cell-penetrating pituitary adenylate cyclase-activating polypeptide (PACAP) for targeted neuronal delivery. The time-resolved synchrotron SAXS study revealed that the PUFA-LNPs exploit the inherent pH-sensitivity of DHA and EPA to undergo a rapid, millisecond-timescale pH-dependent structural transformation from a hexagonal mesophase (lattice parameter shrinkage from 6.14 nm to ~5.57 nm within 200 ms). This dynamic mechanism, triggered by acidic pH, induces a more compact LNP nanostructure that promotes the efficient release of poorly soluble antioxidant compounds. The *in vivo* safety study following intranasal administration in C57BL/6 J mice established excellent biocompatibility for nose-to-brain drug delivery. The multidrug-loaded LC-LNPs induced significant neuroprotective transcriptomic changes, including the upregulation of mitochondrial, antioxidant, and neurotrophic markers alongside suppression of pro-apoptotic genes. The *in vitro* studies confirmed that PUFA-LNPs effectively modulate mitochondrial protein activity (e.g., a 1.5-fold increase in ATP synthase expression), enhance mitochondrial resilience, antioxidant enzyme function (GSH-Px), and positively influence ROS-associated signaling pathways. Thanks to the ionizable carboxyl groups of PUFAs, which confer their intrinsic pH-sensitive properties, we achieved precisely characterized, pH-responsive structural reorganization of the LNPs, enabling enhanced intracellular drug delivery and synergistic neuroprotection of neuronal cells.

## 1. Introduction

Liquid crystalline lipid nanoparticles (LC-LNPs), such as cubosomes and hexosomes, are promising options in nanomedicine for therapy and diagnosis of various diseases as well as vaccine development, making them a versatile nanocarrier platform [1–4]. They offer many advantages, e.g., biocompatibility, biodegradability, and enhanced drug bioavailability, as controlled by cellular uptake and surface functionalization with targeting ligands, peptides, and proteins [1,5–8]. The internal nanoarchitectures of LC-LNPs of cubosomal and hexosomal types are highly ordered and display large interfacial area-volume ratios, which allow for efficient encapsulation and site-specific delivery of a

wide range of functional molecules with different physicochemical properties [1,9–12]. While the successes of the FDA-approved LNP-based mRNA vaccines (e.g., for SARS-CoV-2) and siRNA therapeutics (e.g., Onpattro) are well recognized, the benefits of LC-LNPs over conventional lipid nanoparticles (such as liposomes and solid lipid nanoparticles) remain largely unexplored in nanomedicine development. This is due to limited *in vivo* studies and a lack of sufficient information on their pre-clinical outcomes in delivering diverse cargo types [1,5–8].

A primary obstacle limiting the therapeutic efficacy of nanoparticles within the central nervous system is the challenge of intracellular delivery [6,7]. After cellular uptake, a significant portion of internalized nanocarriers becomes sequestered in the *endo*-lysosomal pathway,

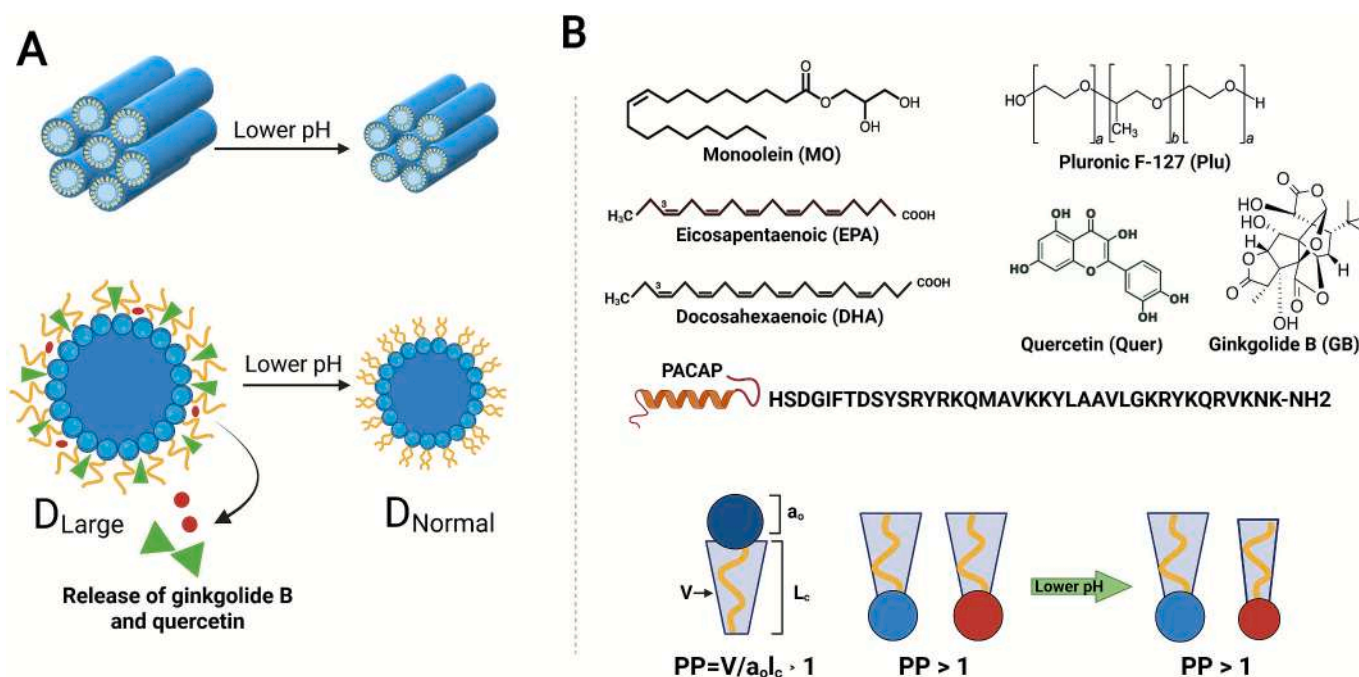


**Fig. 1.** pH-induced structural transition of liquid crystalline PUFA-loaded lipid nanoparticles and impact on the drug release mechanism. (A) Schematic presentation of structural changes of PUFA-hexosome nanocarriers in response to acidic pH. Under physiological pH, PUFA-hexosomes form a highly ordered inverted hexagonal phase with a large channel size ( $D_{Large}$ ) resulting from electrostatic repulsion forces. However, exposure to lower pH can lead to protonation-induced lipid rearrangement, curvature change of the lipid/water interfaces, and particle lattice shrinkage to a smaller channel size ( $D_{Normal}$ ). The latter may cause squeezing out of encapsulated hydrophobic drug molecules (e.g., ginkgolide B and quercetin) from the lipid domain. (B) Chemical structures of ginkgolide B, quercetin, docosahexaenoic acid (DHA), monoolein (MO), Pluronic F127, and pituitary adenylate cyclase-activating polypeptide (PACAP). The ionizable headgroups of DHA are colour-coded (red) to distinguish them from the headgroups of MO (blue), which remain unchanged upon acidification of the microenvironment. MO and DHA promote cone-shaped molecular geometries ( $PP > 1$ ), favouring the inverted hexagonal phase ( $H_{II}$ ) formation. During acidification, the headgroup area and packing of DHA within the internal organization are altered, facilitating a pH-responsive drug release mechanism associated with a change in curvature of the lipid/water interfaces.

where the acidic and enzyme-rich environment leads to cargo degradation and prevents access to cytosolic targets like mitochondria [11,13–18]. Consequently, a key objective in advanced nanocarrier design is the development of systems that can respond to the unique stimuli of the endosomal microenvironment. The progressive acidification of endosomes (from pH  $\sim 7.4$  to  $\sim 5.0$ ) provides a reliable internal trigger for engineering such “smart” nanoparticles. Their pH-response is crucial for inducing LNP structural transitions and facilitating cargo release into the cytosol [13–22].

Omega-3 polyunsaturated fatty acids (PUFAs), such as eicosapentaenoic acid (EPA; c20:5 n-3) and docosahexaenoic acid (DHA, c22:6 n-3), are well-recognized for their potent anti-inflammatory, antioxidant, and neuroprotective bioactivities [7,9,23–30]. The inherent ionizability of DHA and EPA offers a promising means for integrating them as structural components in pH-responsive LNP systems. The rationale of the present study is to examine how EPA and DHA, as ionizable lipids, influence pH-responsive structural transitions within lyotropic liquid crystalline nanoassemblies (Fig. 1) and the drug release behaviour under pH conditions, such as those occurring in endosomal/lysosomal compartments.

The design of our LC-LNPs is based on a multi-targeted synergistic strategy (Fig. 1). We created mixed amphiphilic nanoassemblies of monoolein (MO), forming stable cubic and hexagonal mesophases, enabling the incorporation of  $\omega$ -3 PUFAs with pH-responsive ionizable behaviour. This integration allowed for the modulation of lipid packing and curvature in a pH-dependent manner. We hypothesized that the MO/PUFA nonlamellar structures would be capable of undergoing significant pH-triggered structural transformations. The choice to co-encapsulate ginkgolide B (GB; a key active in *Ginkgo biloba*) and quercetin (Quer; a flavonoid), whose hydrophobic structures are shown in Fig. 1, aimed at achieving synergistic multi-targeted therapeutic effects by targeting complementary pathways involved in mitochondrial protection and oxidative stress reduction. A stimuli-responsive self-assembled lipid system with combined antioxidant, anti-inflammatory, and neuroprotective activities could amplify the therapeutic outcome. Co-encapsulation of the antioxidants GB and Quer (known for their roles in mitochondrial protection and reducing oxidative stress) [31–33] and assembling PUFA-LNPs with pituitary adenylate cyclase-activating polypeptide (PACAP) is expected to further enhance the neurotherapeutic potential through targeted delivery and receptor-mediated uptake (via the PAC1 G-protein-coupled receptor (GPCR)) [34]. However, the flavonoid Quer has a very low release rate at physiological pH, which vastly reduces its bioavailability [35]. We hypothesize that improved cytosolic release of GB and Quer occurs upon a structural transition of PUFA-LNPs in an acidic environment, promoting membrane fusion and drug release.

The novelty of our work lies in the rational design of ionizable  $\omega$ -3 PUFA-based hexosomal nanoassemblies that unify structural responsiveness, therapeutic bioactivity, and targeted delivery within a single platform. Unlike conventional monoolein-based hexosomes or cubosomes, which rely on inert lipids for achieving nonlamellar structural organization, our system leverages the ionizable nature of PUFAs to drive pH-triggered structural change and enhance cytosolic drug release of poorly soluble drugs (key bioactives of *Ginkgo biloba*). In contrast to prior PUFA-containing nonlamellar carriers, which typically incorporate PUFAs as health-beneficial additives, we employ them as core structural elements that actively modulate curvature and internal organization. Moreover, while pH-responsive fatty acid systems have demonstrated curvature switching or ionization-driven transitions (e.g., 2-hydroxyoleic acid), our approach uniquely integrates the nanoassemblies' structural dynamics with synergistic co-delivery of neuroprotective antioxidants (ginkgolide B and quercetin) and PACAP-mediated neuronal targeting. We study how this multi-functional assembly design enables overcoming biological barriers and precise modulation of mitochondrial and antioxidant pathways, offering an advanced strategy for treating oxidative stress-related disorders. To this aim, we

investigate the time-resolved kinetics of the multi-drug-loaded PUFA-based LNPs' structural transformations under acidic conditions, and assess their potential to enhance antioxidant defense and mitochondrial protein activity in support of neuronal function.

## 2. Results

### 2.1. Structural Organization of PUFA-Lipid Nanoassemblies Co-Loaded with Ginkgolide B and Quercetin

PUFA-lipid nanoparticles (PUFA-LNPs) were prepared by self-assembly through hydration and dispersion of thin lipid films consisting of MO-EPA-GB-Quer or MO-DHA-GB-Quer mixtures stabilized by Pluronic F127 (Plu). Synchrotron SAXS patterns of blank LNPs (MO-Plu, MO-DHA-Plu, and MO-EPA-Plu) and LNPs with encapsulated GB and Quer are presented in Fig. 2A–C. Structural data for the nanoassembly of the LNPs with the cell-penetrating peptide PACAP are also presented. The performed SAXS investigation established that the MO-Plu and MO-DHA-Plu LNPs without encapsulated small-molecule bioactives or a neuropeptide display a long-range 3D periodicity of a cubic lattice structure. The Bragg diffraction peaks with  $q$ -vector positions, spaced in the ratio  $\sqrt{2} : \sqrt{4} : \sqrt{6} : \sqrt{8} : \sqrt{10} : \sqrt{12} : \sqrt{14} : \sqrt{16} \dots$ , were assigned to the (110), (200), (211), (220), (310), (222), (321) and (400) reflections of a primitive cubic lattice of the  $Im\bar{3}m$  space group ( $Q^{IP}$ ) (Fig. 2A, blue and purple plots). The cubic lattice parameters were determined to be  $a_Q(Im\bar{3}m) = 16.0 \pm 0.02$  nm and  $20.33 \pm 0.03$  nm for MO-Plu and MO-Plu-DHA LNPs, respectively. The SAXS pattern of the dispersed MO-Plu-EPA LNP system exhibited low-intensity Bragg peaks, which could not be indexed to a well-defined liquid crystalline structure (Fig. 2A). This suggested a tendency for uneven distribution of EPA along the curved bilayer membranes.

Notably, the incorporation of the hydrophobic antioxidants GB and Quer tuned the lipid bilayer properties and stabilized the liquid crystalline supramolecular organization of the dispersed LNPs by inducing the formation of coexisting nonlamellar phases. The inverted hexagonal ( $H_{II}$ ) phase appeared to be the dominant nonlamellar structure for the MO-EPA-Plu-GB-Quer LNP system (Fig. 2B, green plot). The sequence of Bragg peak maxima at  $q_1 = 0.118 \text{ \AA}^{-1}$ ,  $q_2 = 0.204 \text{ \AA}^{-1}$ ,  $q_3 = 0.235 \text{ \AA}^{-1}$  was indexed with  $q$ -vector positions spaced in the ratio 1:  $\sqrt{3}$ : 2. The inverted hexagonal structure was characterized by a unit cell lattice parameter  $a_{(HII)} = 6.17 \pm 0.05$  nm.

The liquid crystalline assemblies of the MO-DHA-Plu-GB-Quer mixture yielded an  $H_{II}$  phase with Bragg peak positions at  $q_1 = 0.119 \text{ \AA}^{-1}$ ,  $q_2 = 0.207 \text{ \AA}^{-1}$ , and  $q_3 = 0.239 \text{ \AA}^{-1}$ , which determined a lattice parameter  $a_{(HII)} = 6.1 \pm 0.05$  nm (Fig. 2C, brown plot). The Bragg peaks of a coexisting cubic structure discerned at low  $q$ -vectors were of quite low intensity, which can be explained by the structural transition of the cubosomes into an  $H_{II}$  phase induced by the incorporation of guest molecules.

To achieve nose-to-brain targeted delivery, a separate set of nanoparticles was functionalized with the neurotrophic pituitary adenylate cyclase-activating polypeptide (PACAP). The functionalization of the PUFA-LNPs by PACAP was done by the post-insertion method. The electrostatic adsorption and complexation of the positively charged peptide (PACAP MW 4535 Da, net charge +9.1 at pH 7) on the exposed interfaces of the lipid nanoparticles was almost instantaneous. The association efficiency was above  $95 \pm 5\%$ , as evidenced by the negligibly small amount of PACAP in the supernatant following complexation. The incorporation of PACAP significantly influenced the structural organization of the MO-EPA-Plu-GB-Quer and MO-DHA-Plu-GB-Quer nanocarriers. Figs. 2B and C (olive green and orange plots) present the SAXS pattern of the MO-EPA-Plu-GB-Quer and MO-DHA-Plu-GB-Quer LNPs associated with PACAP. The coexistence of  $H_{II}$  and gyroid  $Ia3d$  was observed with an estimated  $H_{II}$  lattice of  $a_{(HII)} = 6.11 \pm 0.05$  and  $5.97 \pm 0.05$  nm and cubic  $Ia3d$  lattice parameters of  $a_{Q(Ia3d)} = 12.89 \pm 0.02$  and  $12.63 \pm 0.02$  nm, respectively (Fig. 2B and C; orange and blue arrows



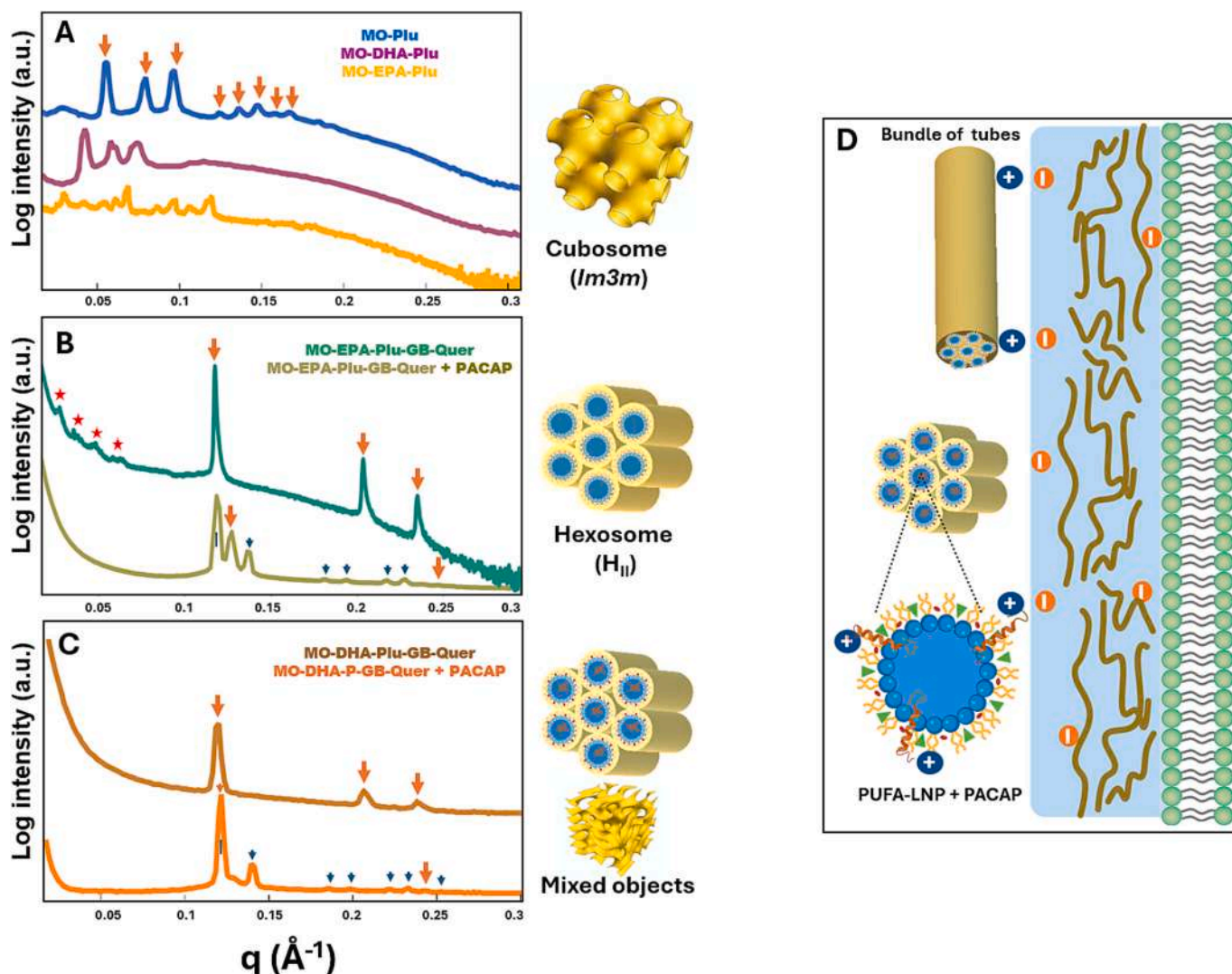


**Fig. 2.** Synchrotron small-angle X-ray scattering (SAXS) patterns of multi-functional lyotropic liquid crystalline nanoparticles designed for neurological disorder treatment and a simplified scheme of the biological barrier interface upon nose-to-brain delivery. (A) SAXS patterns of nanoassemblies of monoolein stabilized by Pluronic F127 (MO-Plu) in excess aqueous medium and monoolein-Pluronic mixtures encapsulating DHA or EPA (MO-DHA-Plu/MO-EPA-Plu). (B, C) Liquid crystalline nanoparticles of the hexosome type obtained by encapsulating ginkgolide B (GB) and quercetin (Quer) within mixed nanodispersions (MO-EPA-Plu-GB-Quer or MO-EPA-Plu-GB-Quer) or functionalized with the peptide PACAP (MO-EPA-Plu-GB-Quer + PACAP/ MO-DHA-Plu-GB-Quer + PACAP). The SAXS patterns were acquired at a temperature of 22 °C. The arrows indicate the positions of the Bragg diffraction peaks. (D) Schematic presentation of the biological interface created by the negatively charged mucus layer during nose-to-brain delivery. A pH  $\sim$ 5 is considered physiologically relevant, particularly in the mucosal surface layer, where ionizable lipids and peptides encounter the extracellular milieu during intranasal delivery. Ionizable hexosomes as LNPs with asymmetrical (elongated) shapes are designed to favor the retention of the multi-drug-loaded LNPs at the interface of the mucin network. The positively charged PACAP peptide molecules exposed at the hexosome's interfaces can favor LNP mucoadhesion and enhanced penetration of the co-delivered synergistic therapeutics.

represent Bragg diffraction peak positions of  $H_{II}$  and  $Ia3d$ ). The coexistence of the inverse hexagonal and cubic  $Ia3d$  phases reflects a complex internal structure. Evidently, electrostatic interactions with PACAP modify the curvature of the lipid/water interfaces as well as their hydration state. Due to the excess of lipid phase (monoolein, EPA/DHA) relative to PACAP, the available amount of bound peptide may induce small fractions of alternative phases (such as cubic or inverted-hexagonal domains) with distinct lattice spacings and hydration profiles, likely driven by local changes in hydration and electrostatic environment.

## 2.2. Structural Dynamics of pH-Responsive PUFA-GB-Quer-Loaded Hexosomes

We employed time-resolved small-angle X-ray scattering (TR-SAXS) with a millisecond timescale (5 ms) resolution to investigate the kinetics

of structure evolution of LNPs driven by pH changes. This technique allowed us to capture the dynamic structural changes of the nanoparticles under acidic conditions. Considering the pH value around 5.0 in the nasal epithelium environment, we examined whether the pH effect on the structural behaviour of the nanoparticles may promote intranasal drug delivery, particularly targeting the brain. We focused on the structural response of the PUFA-LNPs at pH 5.0, which mimics the acidic microenvironments of intracellular compartments (e.g., endosomes/lysosomes) and may also approximate the localized acidosis observed during severe neuroinflammation or oxidative stress [36,37].

We selected PUFA-LNPs, comprising MO-DHA-Plu-GB-Quer, for time-resolved structural studies as a drug delivery system. This formulation was chosen because the MO-DHA-Plu-GB-Quer self-assembled mixture formed a well-defined inverted hexagonal phase in excess aqueous medium, as revealed by the static SAXS plots (Fig. 2B and C). For *in situ* rapid mixing experiments on pH-dependent LNP transitions,

pre-made MO-DHA-Plu-GB-Quer LNPs were rapidly mixed with sodium dihydrogen phosphate buffer salt buffer (200 mM) containing 0.2 % HCl (v/v) at a flow rate mixing ratio of 1:1 (v/v).

Upon rapid mixing with an acidic buffer, MO-DHA-Plu-GB-Quer LNPs exhibited an initial kinetic pathway involving the evolution of sharp Bragg peaks characteristic of the inverted hexagonal ( $H_{II}$ ) phase within less than 200 ms at pH 5.0. Time-resolved SAXS experiments with an unprecedented 5 ms temporal resolution captured the dynamic kinetics of the structural transformations. This included the splitting and shifting of diffraction peaks, indicating a rapid shrinkage of the hexagonal lattice (from  $a_{(HII)} = 6.14 \pm 0.05$  nm to  $\sim 5.58 \pm 0.05$  nm) and the formation of distinct coexisting  $H_{II}$  domains, consistent with phase dehydration and payload release.

Time-resolved SAXS patterns during the mixing of LNPs (MO-DHA-Plu-GB-Quer) with the acidic buffer solution are presented in Figs. 3A-D. They show nanoparticles' *in situ* structural evolution over time, where the scattering profiles are presented sequentially from bottom (pH 7.4) to top (pH 5.0). We observe an initial kinetic pathway of sharp Bragg's diffraction peaks of the inverse hexagonal phase, with intermediate structures formed with the disappearance and reappearance of the (11) and (20) reflections of the inverse hexagonal phase. The peak position

also exhibited a slight shift towards high  $q$ -values during the structural evolution (towards reaching equilibrium), indicating a compression or shrinkage of the hexagonal phase and inducing the release of the therapeutic compound (Fig. 1 A). Two distinct inverse hexagonal phases, which depict transitions from a more homogeneous phase to distinct sub-populations with slightly varied packing densities and different lattice parameters at low pH, were also observed (Fig. 3D). The first and second hexagonal phases after the pH mix yielded  $q$  maxima positions at  $q_1 = 0.127/0.130 \text{ \AA}^{-1}$ ,  $q_2 = 0.220/0.225 \text{ \AA}^{-1}$ , and  $q_3 = 0.254/0.260 \text{ \AA}^{-1}$ . The sequence of Bragg peak maxima for the original PUFA-LNPs in excess aqueous phase was resolved at  $q_1 = 0.118 \text{ \AA}^{-1}$ ,  $q_2 = 0.204 \text{ \AA}^{-1}$ ,  $q_3 = 0.236 \text{ \AA}^{-1}$  with a lattice parameter of  $a_{(HII)} = 6.14 \pm 0.05$  nm (Fig. 3D, blue plot). The decrease in pH caused a shift in the Bragg peak positions of the  $H_{II}$  phases, leading to smaller aqueous channels (*i.e.*, curvature change), thus resulting in a smaller lattice parameter of  $a_{(HII)} = 5.73 \pm 0.05$  and  $5.57 \pm 0.05$  nm (see the black and blue arrows on Fig. 3D, orange plot).

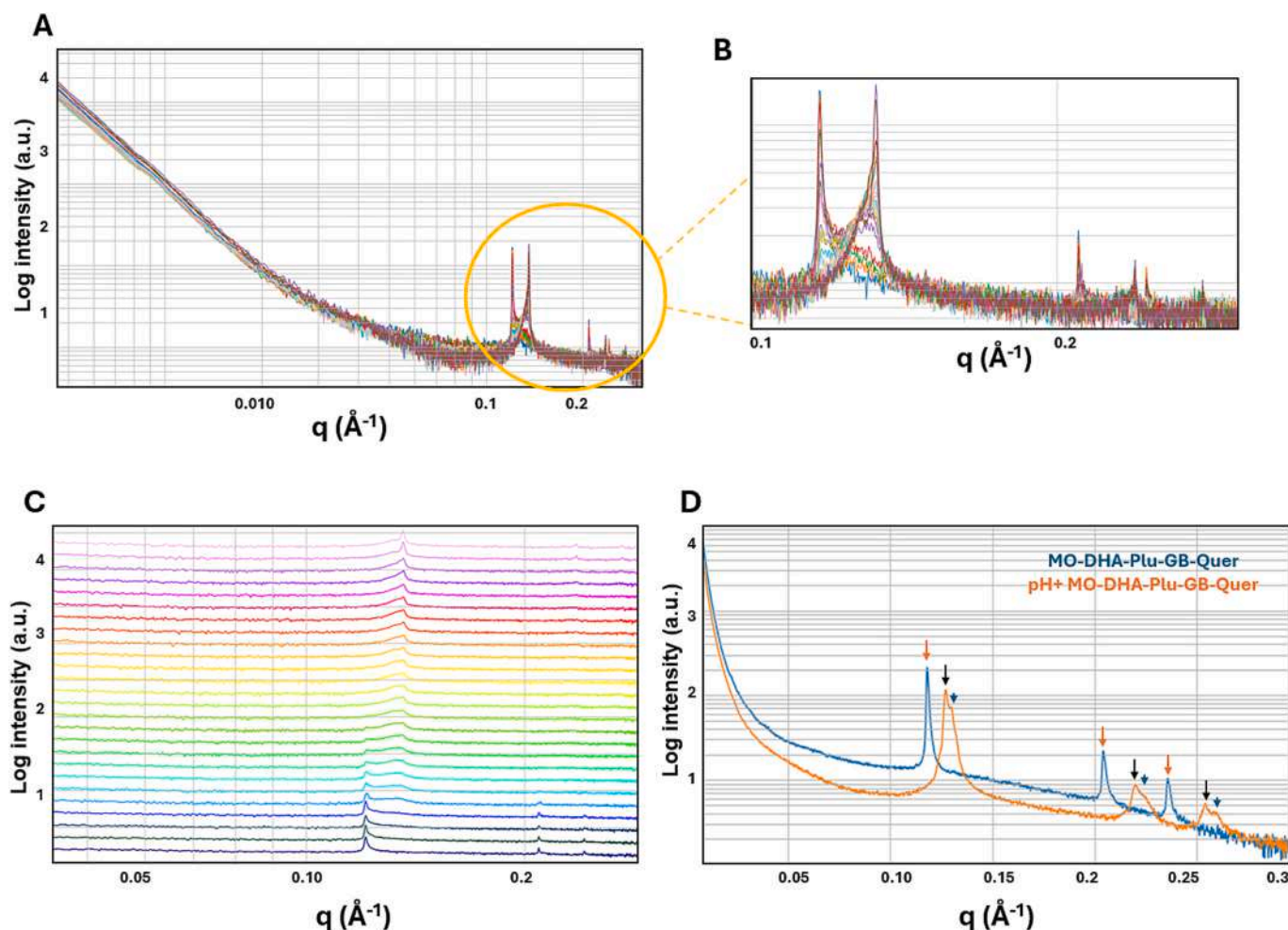


**Fig. 3.** Dynamic patterns of pH-dependent time-resolved (TR) SAXS curves for antioxidant-loaded liquid crystalline PUFA nanoparticles. (A) TR-SAXS profiles (obtained at 5 ms resolution) following rapid stopped-flow mixing of MO-DHA-Plu-GB-Quer LNPs with acidic buffer, showing the overall time-dependent behaviour of an inner inverted hexagonal ( $H_{II}$ ) structure. (B) Magnified view of the characteristic  $q$ -region from panel A, highlighting the peak splitting and peak shifts, indicative of structural rearrangements of the  $H_{II}$ -phase structure. (C) A time-resolved sequence of SAXS profiles demonstrating the transition pathway of the hexosome LNPs (s). Panels (A-C) provide an integrated depiction of the LNP transformation process, from global structural trends to fine-scale rearrangements and transition dynamics. (D) SAXS plots comparing the initial LNP structure at neutral pH (blue plot) with the final structure at acidic pH (orange plot), showing the appearance of new Bragg peaks, peak splitting, and a shift towards higher  $q$ -values consistent with  $H_{II}$ -phase dehydration and formation of coexisting  $H_{II}$ -phase domains. (For interpretation of the references to colour in this figure legend, the reader is referred to the web version of this article.)

### 2.3. Selective Cargo Release Triggered by pH-Induced Structural Reorganization of PUFA-LNPs

The pH-triggered structural transformation directly correlated with the LNPs' ability to release their cargo. To examine the release profile of encapsulated antioxidants from hexosomal nanocarriers, we quantified the cumulative drug release from PUFA nanoparticles under pH conditions mimicking those of the endosomal or mucosal microenvironment. It is hypothesized that acidification (pH 5–6) may enhance the release of hydrophobic cargo from MO/PUFA hexosomes, potentially as a consequence of nonlamellar reorganization. Quercetin (Quer) and ginkgolide B partition deeply into the hydrophobic domains of the nanocarriers, making their release kinetics an acid-driven structural-transition dependent.

Fig. 4 depicts the quantitative release profiles of Quer, determined by an HPLC method, in release media with pH 5.0 and pH 7.4 (PBS). Using the dialysis method, approximately 12 % of the encapsulated cargo was released within the first hour at pH 5.0, increasing to 37 % after 24 h (Fig. 4, green bars). The accelerated liberation of encapsulated antioxidant molecules under acidic conditions supports the hypothesis that acidification can trigger a stimulus-responsive release of therapeutic agents from the nanoparticles that have been internalized. Moreover, it can favor its subsequent effects on mitochondrial function driven by the membrane potential changes ( $\Delta\Psi$ ). At physiological pH 7.4, quercetin release from nanocarriers was negligible (less than 5 %) even after 50 h (Fig. 4, blue bars).

Accurate quantification of ginkgolide B (GB) release by HPLC was hindered by its weak chromophores, low analytical sensitivity, and complex elution profile, which compromised reliable detection.

Overall, the *in vitro* release study demonstrated that at physiological pH 7.4, the release of the encapsulated antioxidant (Quer) was negligible. However, upon exposure to an acidic medium of pH 5.0, a significant and sustained release was initiated. This confirms that the LNP structural change induced by the acidic pH effectively favors the cargo release.

### 2.4. Regenerative Effects of PUFA-GB-Quer-Loaded Nanoassemblies Functionalized with PACAP on an In Vitro Oxidative Stress Model

#### 2.4.1. PUFA-LNPs Promote Neuronal Recovery and Exhibit Composition-Dependent Cytoprotective Effects

To assess the neuroprotective potential of our pH-responsive PUFA-

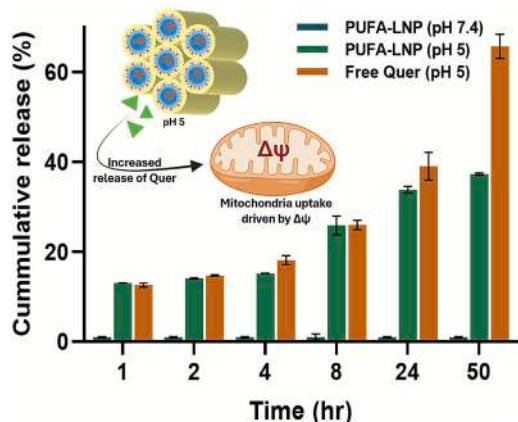


**Fig. 4.** pH-responsive release of quercetin from PUFA-LNPs. Cumulative release profiles of Quer from PUFA-Quer-LNPs evaluated by the dialysis method under physiological pH 7.4 (blue bars) and pH 5.0 (endosomal/lysosomal pH, green bars) conditions over 50 h *versus* free Quer suspension at pH 5.0 (orange bars). Under acidic conditions, free Quer exhibits faster dissolution compared to PUFA-Quer-LNPs, whereas negligible drug release (less than 5 %) was observed at physiological pH. Data are represented as mean  $\pm$  SD ( $n = 3$ ).

LNPs, SH-SY5Y cells were differentiated and subjected to potassium persulfate (KPS)-induced oxidative stress. For this, SH-SY5Y cells were differentiated for 5 days, and living cells' cellular morphology was visualized on days 3 and 5. The differentiated cells were treated with 50 mM KPS for 30 min to induce oxidative stress damage and subsequently treated with either the blank nanocarrier (MO-Plu) or PUFA-GB-Quer-loaded LNPs. The exposure of SH-SY5Y cells to retinoic acid for 5 days led to a neuronal-like phenotype characterized by the extension of short, unbranched neurites. The treatment with PUFA-LNPs, co-encapsulating GB and Quer, led to notable improvements in neuronal morphology compared to KPS-stressed controls (Fig. 5A). Specifically, cells treated with MO-DHA-Plu-GB-Quer LNPs displayed extensive, branched neurite outgrowth, superior to that observed with MO-EPA-Plu-GB-Quer or blank MO-Plu nanocarriers, suggesting a profound regenerative capacity of the LC-LNPs.

Initial safety evaluations indicated that both MO-EPA-Plu-GB-Quer and MO-DHA-Plu-GB-Quer MO-EPA LNPs, as well as blank MO-Plu cubosomes, were well-tolerated at concentrations relevant for neuroprotective studies, even slightly enhancing viability compared to RA/FBS(–) control (MO-EPA-Plu-GB-Quer,  $p = 0.114$  and the blank MO-Plu,  $p = 0.587$ ) (Fig. 5B). However, dose-dependent cytotoxicity revealed that MO-EPA-Plu-GB-Quer LNPs exhibited higher toxicity at concentrations  $\geq 200 \mu\text{M}$  compared to MO-DHA-Plu-GB-Quer LNPs (Fig. 5C), guiding the selection of non-toxic doses for subsequent mechanistic investigations. These morphological and viability data evidence the potential of PUFA-LNPs to boost neuronal recovery, with DHA-containing formulations showing more pronounced neurite extension and a narrower therapeutic window at high concentrations.

#### 2.4.2. PUFA-LNPs Attenuate Oxidative Stress and Restore Mitochondrial Function via Antioxidant Payload Delivery

Given the central role of oxidative stress and mitochondrial dysfunction in neurodegeneration, we investigated the impact of PUFA-LNPs on these parameters. Following KPS-induced oxidative stress, cellular treatment with DHA-formulated LNPs (MO-DHA-Plu-GB-Quer) significantly scavenged intracellular ROS to a greater extent than EPA-formulations (Fig. 5D). *In vitro*, DCFH-DA and JC-10 assays were performed to examine this. Furthermore, both MO-PUFA(EPA/DHA)-GB-Quer-loaded LNPs enhanced mitochondrial function compared to the KPS control (Fig. 5E). The superior ROS reduction correlated with a marked enhancement of mitochondrial membrane potential changes ( $\Delta\Psi$ ) by both MO-PUFA(EPA/DHA)-GB-Quer-loaded LNPs compared to KPS-stressed controls (Fig. 5E).

Since tyrosine hydroxylase (TH) is the rate-limiting enzyme in the catecholamine synthesis pathway, responsible for regulating dopamine, epinephrine, and norepinephrine levels in tissues, we conducted cell-based ELISA experiments to assess the protein-level variations of this enzyme. As shown in Fig. 5F, TH levels are significantly upregulated in cells treated with MO-DHA-Plu-GB-Quer compared to the KPS-induced oxidative stress model and the blank nanocarrier (MO-Plu). On the other hand, the MO-EPA-Plu-GB-Quer cubosome nanostructure showed a slightly higher but insignificant increase in TH protein expression. These results indicate that ROS production, accompanied by mitochondrial dysfunction, may play a role in the effectiveness of nanoparticle treatment on neurite production. The increase in TH levels facilitated by the LNPs could potentially alleviate the loss of dopaminergic neurons associated with oxidative stress conditions, consequently increasing TH expression. Thus, the enhanced expression of tyrosine hydroxylase, particularly by MO-DHA-Plu-GB-Quer LNPs (Fig. 5F), supported the alleviation of ROS-induced neuronal cell dysfunction.

### 2.5. Internalization Kinetics of PUFA-LNPs Before and After Functionalization with PACAP

Using flow cytometry, we investigated the kinetics of internalization



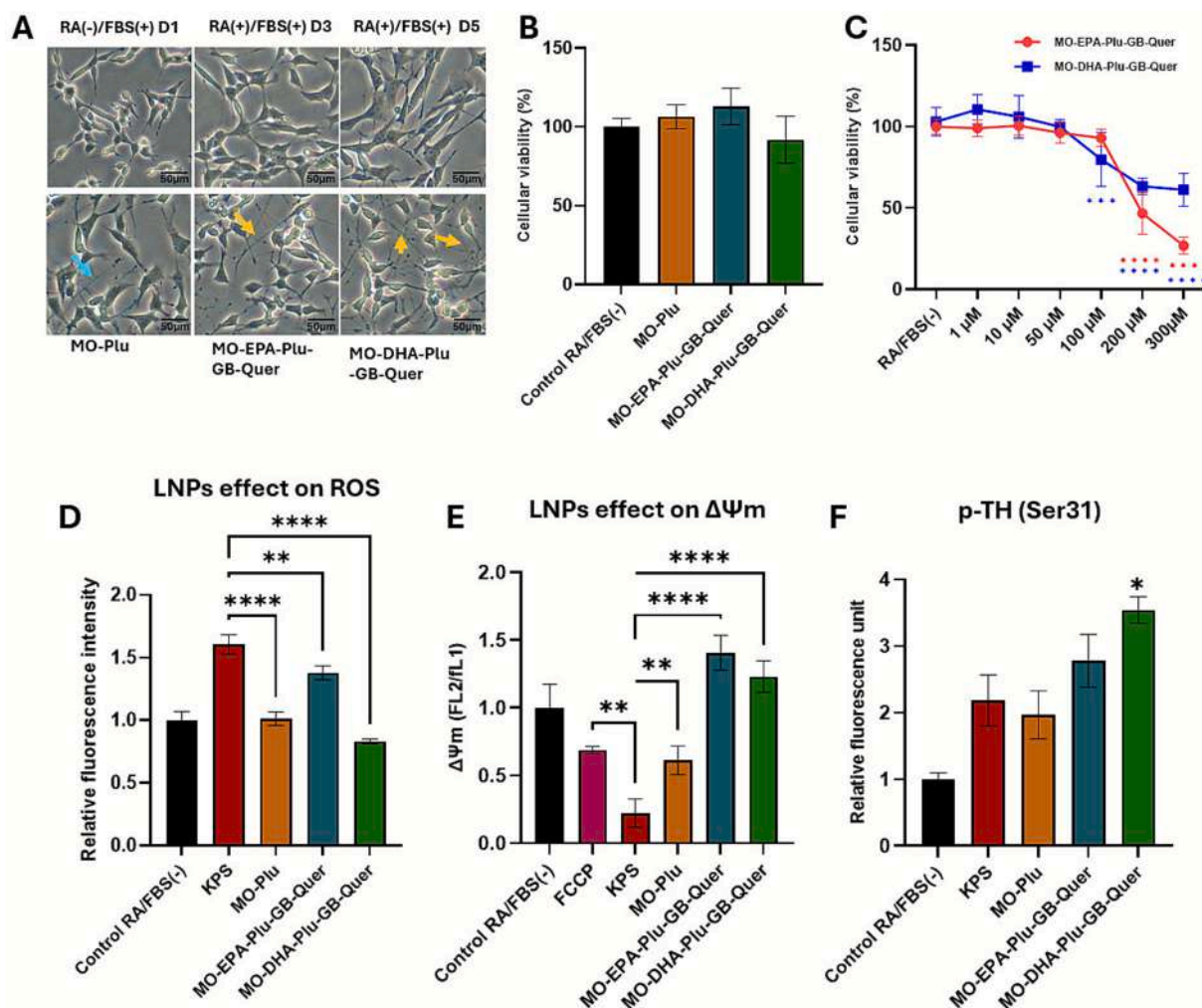


**Fig. 5.** Cellular responses to PUFA-LNP treatment of differentiated SH-SY5Y cells under oxidative stress conditions. (A) Morphology of SH-SY5Y cells treated with MO-Plu, MO-EPA-Plu-GB-Quer, or MO-DHA-Plu-GB-Quer for 24 h in RA/FBS(-) cell culture medium. The yellow and blue arrows indicate short and elongated neurite outgrowth, respectively. (B, C) Quantification of cell viability and dose-dependent cell effect in response to increasing concentrations of MO-EPA-Plu-GB-Quer and MO-DHA-Plu-GB-Quer (1–300  $\mu$ M) LNPs, assessed via MTT assay. Cytotoxicity arises in the high concentration range of 200–300  $\mu$ M. Data are represented as mean  $\pm$  SD ( $n = 6$ , \*\*\* $p = 0.0004$ , \*\*\*\* $p < 0.0001$  vs KPS). (D, E) Relative intracellular ROS ( $n = 3$ , \*\* $p = 0.0025$ , \*\*\*\* $p < 0.0001$ ) and mitochondrial membrane potential changes ( $\Delta\Psi_m$ ) were assessed by flow cytometry using a DCFH-DA probe and JC-10 staining. Data are represented as mean  $\pm$  SD ( $n = 3$ , \*\* $p =$ , \*\*\*\* $p < 0.0001$  vs KPS control). (F) Relative expression of tyrosine hydroxylase phosphorylated at Ser31 (p-TH Ser31), a marker of dopaminergic function and neuroprotection, determined by ELISA ( $n = 3$ , \* $p = 0.0366$ ). (For interpretation of the references to colour in this figure legend, the reader is referred to the web version of this article.)

of MO-DHA-GB-Quer-loaded LNPs alone or with bound cell-penetrating neurotrophic peptide PACAP in differentiated SH-SY5Y cells. Fig. 6(A, B) compares the time-dependent internalization curves of fluorescent Rhod-labeled LNPs (Rhod-LNP) and LNPs with a bound PACAP-TAMRA fluorescent conjugate (TAMRA-LNP), where TAMRA is tetramethylrhodamine and Rhod is 1,2-dioleoyl-sn-glycero-3-phosphoethanolamine-N-(lissamine rhodamine B sulfonyl) moiety. The internalization kinetics of TAMRA-LNPs showed a continuous increase from 2 to 24 h, with a profound internalization between 6 and 24 h. In contrast, TAMRA-PACAP uptake tended to plateau over extended exposure times between 6 and 24 h. This suggests that TAMRA-LNPs may exhibit enhanced and sustained cellular uptake compared to the PACAP-conjugate, particularly over extended incubation periods.

The highest internalization for Rhod-LNPs was observed after 24 h incubation, indicating that the LNPs lacking a cell-penetrating peptide (such as the positively charged PACAP) require extended exposure time to achieve maximum cellular uptake. The considerably higher fluorescence intensity ratios of the Rhod-LNPs in comparison to the unbound PACAP-TAMRA conjugate confirmed the enhanced uptake of the

investigated PUFA-LNPs. These results suggest that PUFA-LNPs are efficiently taken up by cells in a time-dependent manner, with prolonged exposure leading to optimal internalization. This may be essential for achieving a sustained release effect of the therapeutic agents.

The internalization results with the LNPs with bound cell-penetrating neurotrophic peptide PACAP will be exploited for *in vivo* studies targeting the nose-to-brain pathways.

## 2.6. PUFA-GB-Quer-Loaded Hexosomal LNPs Increase the Expression of the Mitochondrial ATP Synthase Protein and the Antioxidant Enzyme GSH-Px Activity

We evaluated the effect of PUFA-GB-Quer-loaded hexosomes and blank LNPs on the regulation of the mitochondrial proteins ATP synthase and the antioxidant enzyme GSH-Px in differentiated SH-SY5Y cells. The results established an increase in ATP synthase expression in response to treatment, particularly for the MO-EPA-Plu-GB-Quer LNP formulation, which slightly outperformed the MO-DHA-Plu-GB-Quer hexosomes (Fig. 6D). These data corroborate the kinetic evolution of

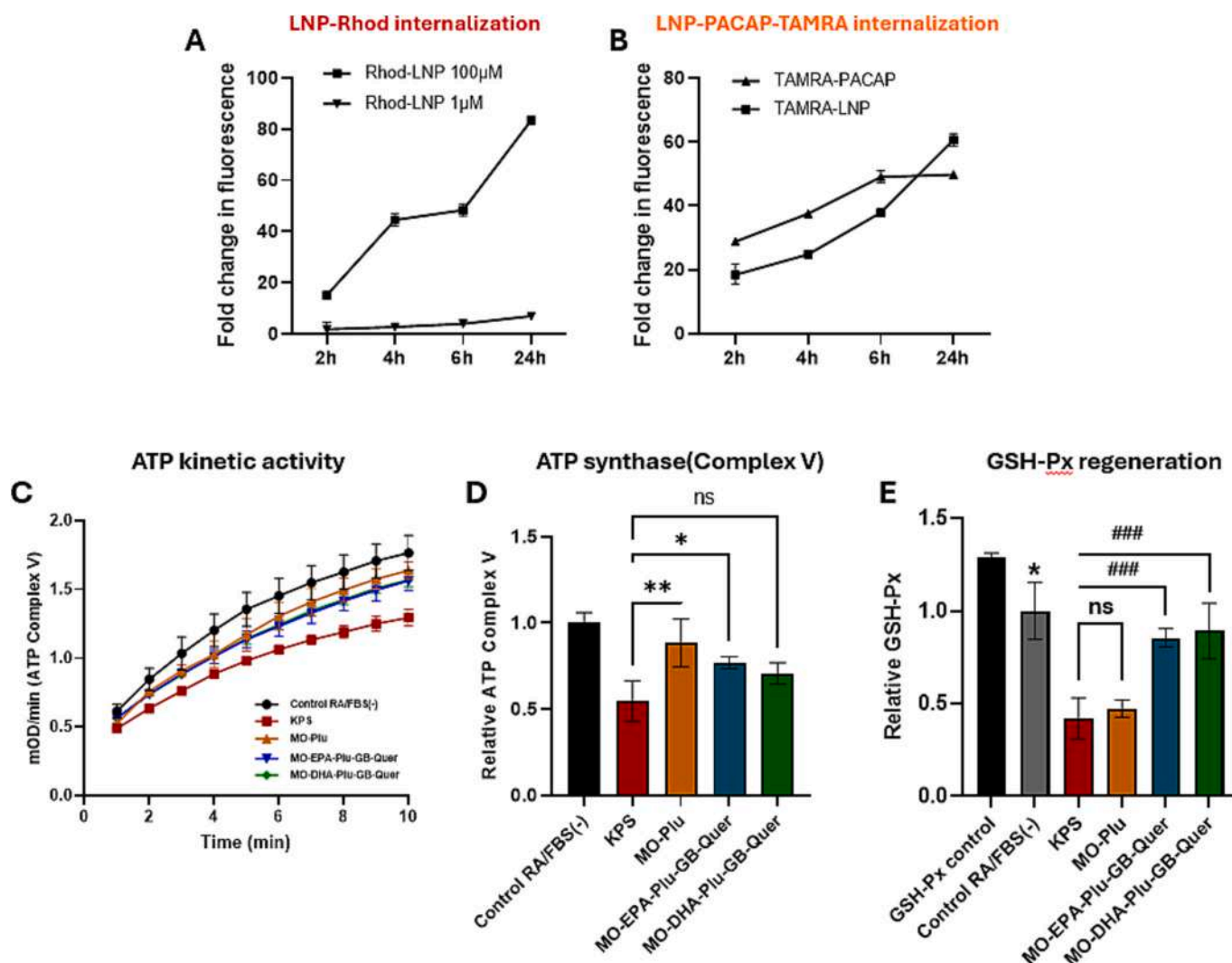


**Fig. 6.** Internalization kinetics of PUFA-LNPs and their mitochondrial effects in differentiated SH-SY5Y cells. (A) Fluorescence intensity changes determined by flow cytometry upon cellular internalization of Rhodamine-labeled hexosomes (100  $\mu$ M and 1  $\mu$ M Rhod-LNP). (B) Cellular uptake of fluorescent PACAP-TAMRA conjugate (5  $\mu$ M) and LNPs with bound fluorescent PACAP-TAMRA (TAMRA-LNP) in differentiated SH-SY5Y cells at different incubation times: 2 h, 4 h, 6 h, and 24 h. To mitigate spectral overlap and ensure reliable detection, the two dyes were selected with distinct excitation/emission profiles. Fluorescence intensities were acquired at the FL2 and FL3 channels for the Rhodamine (Rhod)/TAMRA (tetramethylrhodamine) dyes, respectively. (C) Quantification of ATP synthase (Complex V) protein expression levels by ELISA following PUFA-LNP treatment of SH-SY5Y cells, which were pre-exposed to oxidative stress (KPS). (D) ATP synthase activity over time (0–10 min) in LNP-treated cells. Results are reported as mean  $\pm$  SD ( $n = 3$ ,  $*p = 0.0415$ ,  $**p = 0.0037$ ,  $ns = 0.1618$ ). (E) Glutathione peroxidase (GSH-Px) regeneration levels and improvement of GSH-Px activity after PUFA-LNPs treatment of cells pre-exposed to oxidative stress. Data are reported as mean  $\pm$  SD ( $n = 3$ ,  $ns = 0.9494$ ,  $*p = 0.0181$ ,  $###p = 0.0010$  and  $0.0005$  for MO-EPA-Plu-GB-Quer and MO-DHA-Plu-GB-Quer groups).

ATP synthase activity depicted in Fig. 6C. The increased ATP synthase (Complex V) protein levels and activity (Fig. 6C,D) were consistent with the LNP-mediated restoration of mitochondrial integrity. These findings strongly suggested that the pH-responsive PUFA-LNPs efficiently deliver their antioxidant cargo (GB and Quer) intracellularly, leading to robust mitigation of oxidative damage, a positive effect on metabolic function, and restoration of key mitochondrial functions critical for neuronal survival.

Next, we conducted parallel experiments to determine potential changes in the cellular redox status by measuring the activity of one of the key antioxidant defense enzymes, glutathione peroxidase (GSH-Px). As shown in Fig. 6E, treatment with PUFA-GB-Quer-loaded LNPs for 24 h following KPS exposure significantly upregulated glutathione peroxidase activity as compared to the oxidative stress condition (i.e., the KPS control). This suggested that the formulated PUFA-LNPs effectively enhance the antioxidant defense system by counteracting ROS generation following acute cell exposure to KPS-induced oxidative damage.

## 2.7. PUFA-GB-Quer-Loaded LNPs Modulate Key Neuroprotective Signaling Pathways

### 2.7.1. Effect of PUFA-GB-Quer Cubosomes and Hexosomes on AKT/ERK/CREB Phosphorylation

To elucidate the downstream molecular mechanisms, we examined the effect of PUFA-LNP treatment on critical neurotrophic and survival signaling pathways. Both MO-EPA-GB-Quer and MO-DHA-GB-Quer LNPs upregulated the phosphorylation of AKT and CREB compared to KPS-stressed cells (Fig. 7A, C). Notably, MO-EPA-Plu-GB-Quer LNPs induced a more pronounced phosphorylation of ERK (Fig. 7B), suggesting that different PUFA formulations may engage distinct arms of the neuroprotective signaling network. The upregulation of these pathways, known to be crucial for neuronal survival, differentiation, and plasticity, was consistent with the observed morphological recovery and antioxidant effects following PUFA-LNPs treatment (Fig. 5).



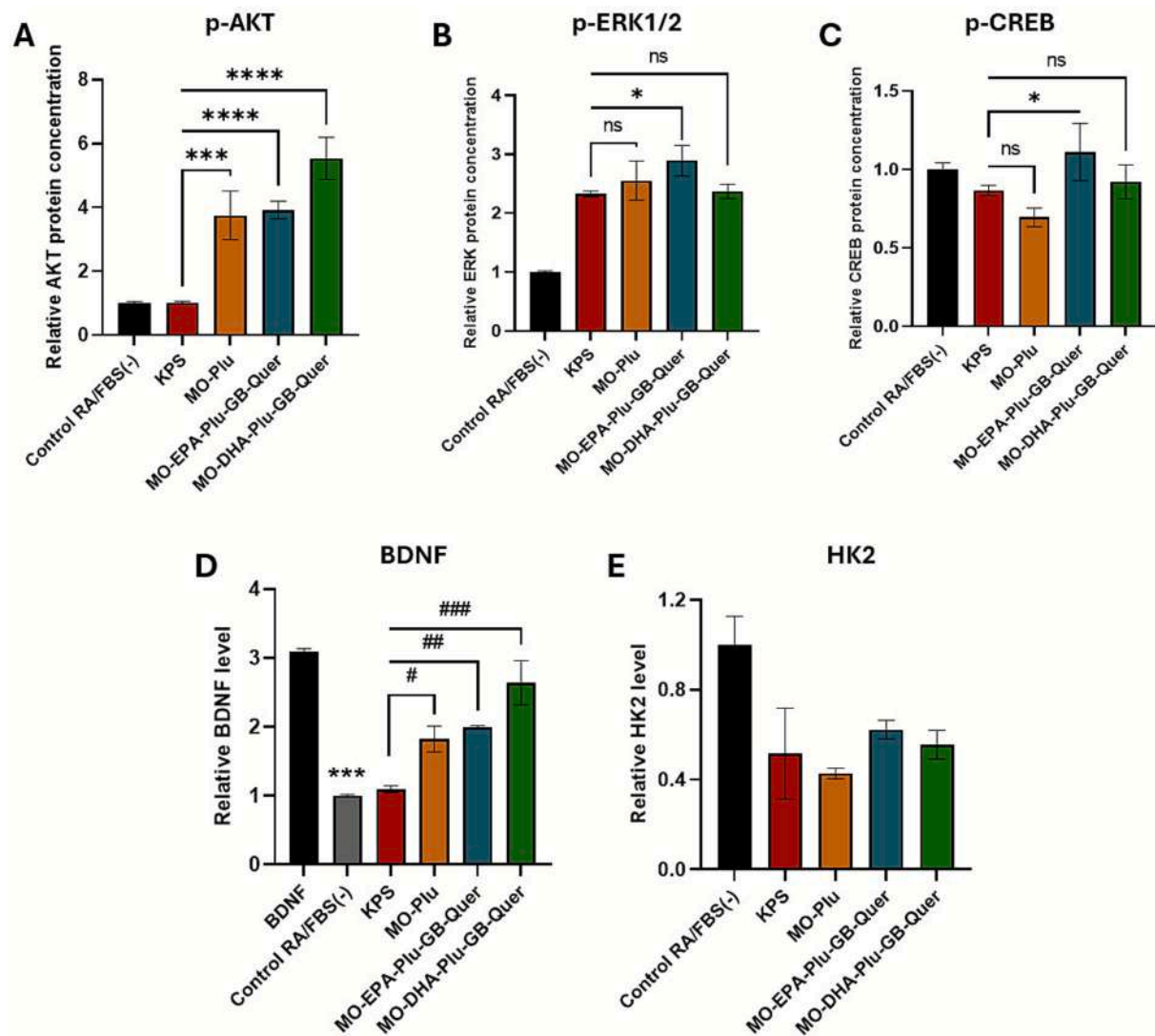


**Fig. 7.** Effect of PUFA-LNPs on recovery of neuronal survival signaling, neurotrophic factor (BDNF) expression, and anti-apoptotic hexokinase-2 mitochondrial protein levels in SH-SY5Y cells pre-exposed to oxidative stress. (A-C) Quantification of phosphorylated AKT (p-AKT), ERK1/2 (p-ERK1/2), and CREB (p-CREB) after treatment with the PUFA-LNPs. Results are presented as mean  $\pm$  SD ( $n = 3$ ,  $ns > 0.05$ ,  $*p < 0.05$ ,  $***p = 0.001$ ,  $****p < 0.0001$  compared to KPS control). (D, E) Brain-derived neurotrophic factor (BDNF) and Hexokinase-2 (HK2) protein expression levels after treatment with the PUFA-LNPs. Results are presented as mean  $\pm$  SD ( $n = 3$ ,  $****p < 0.0001$  vs BDNF group and  $\#p = 0.0114$ ,  $##p = 0.0040$ ,  $###p = 0.0002$  compared to KPS control).

#### 2.7.2. Effect of PUFA-GB-Quer-loaded LNPs on Brain-Derived Neurotrophic Factor (BDNF) and Anti-Apoptotic Hexokinase-2 (HK2) protein expression levels

Fig. 7D and E reveal the increased BDNF protein levels as well as the enhanced Hexokinase-2 mitochondrial protein expression after PUFA-LNPs treatment of the investigated cellular model. The results obtained demonstrated the potential of the different nanoparticles (MO-EPA-Plu-GB-Quer and MO-DHA-Plu-GB-Quer) to modulate distinct neuroprotective signaling pathways to maintain redox homeostasis. They were quite distinct for ERK and BDNF expression, while MO-DHA-Plu-GB-Quer LNPs efficiently favoured the p-AKT/BDNF signaling pathway.

Additionally, the regulation of the anti-apoptotic mitochondrial protein Hexokinase-2 (Fig. 7E) by PUFA-LNPs, implies a favorable effect on mitochondrial biogenesis and function. These results highlighted the capacity of the PUFA-LNPs not only to deliver antioxidants but also to actively promote pro-survival signaling cascades within stressed neurons.

#### 2.8. Nose-to-Brain Drug Delivery by PUFA-LNPs is Biocompatible and Induces Widespread Neuroprotective Gene Expression Changes in the Brain

Intranasal (IN) administration route offers a non-invasive method for bypassing the blood-brain barrier (BBB) by exploiting direct nose-to-brain pathways (e.g., via the olfactory and trigeminal nerves). The IN route was chosen for *in vivo* safety studies of the PUFA-LNPs, considering that it is a promising strategy for delivering therapeutics to the CNS while avoiding systemic side effects.

##### 2.8.1. Histological Analysis

MO-EPA-Plu-GB-Quer LNPs, functionalized with PACAP, were administered intranasally to C57BL/6 J mice once per week over a 21-day period to evaluate their *in vivo* safety and therapeutic potential as a leading  $\omega$ -3 PUFA formulation. Histological analysis of brain tissue sections from control and LNP-treated samples was performed to evaluate brain tissue integrity across multiple regions, including the cortex, hippocampus, cerebellum, and substantia nigra using Hematoxylin and Eosin (H&E) staining. C57BL/6JGpt mice were intranasally administered with MO-EPA-Plu-GB-Quer LNPs, while control mice received PBS.

The results in Fig. 8A show intact tissue architecture in both control and LNP-treated groups. The control group displayed uniform nuclear distribution and minimal extracellular space, while the LNP-treated group exhibited similar features, with minor glial hyperplasia and irregular cortical layering. No signs of cell loss, inflammation, or structural disruption were apparent. These results suggest that the MO-EPA-Plu-GB-Quer nanoparticles did not induce significant histological toxicity *in vivo*. Our investigation confirmed the excellent biocompatibility of the PUFA-LNP formulation through the chosen non-invasive delivery route.

### 2.8.2. Transcriptomic Profiling Using RNA-Seq Analysis of Brain Tissue Following Intranasal Administration of PUFA-GB-Quer-Loaded Lipid Nanoparticles

Further to the established safety profile, a comprehensive RNA-seq analysis was performed to elucidate the molecular impact of LNP treatment on brain tissue (Fig. 8B-E). Raw sequencing data were processed with Hisat2, StringTie, and DESeq2 packages, following the experimental protocol. The transcriptomic analysis provided detailed insights into the brain tissue responses to LNP treatment, highlighting

genes with significant expression changes. A volcano plot was generated to visualize the differential expression between control and LNP-treated samples (Fig. 8E). The analysis revealed a total of 625 differentially expressed genes (DEGs) with  $p$ -values  $\leq 0.05$ . Among these, 273 genes were upregulated, and 352 genes were downregulated in the LNP-treated group compared to the control, while 24,594 genes showed no significant change in expression.

Additionally, Principal Component Analysis (PCA) was conducted to assess global transcriptional differences between the control and LNP-treated groups (Fig. 8F). The samples from LNP-treated mice (LNP-552, LNP-570, LNP-577) exhibited moderate cohesion between samples, whereas the control samples (Ctrl-520, Ctrl-524, Ctrl-517) were more dispersed. The PCA plot demonstrated distinct clustering, with PC1 and PC2 accounting for 23.72 % and 21.46 % of the variance. This indicated a significant and consistent transcriptional response to the LNP-based nanomedicines (Fig. 8F).

Further analysis focused on genes related to mitochondrial function, oxidative stress, and neuronal survival. The heatmap results revealed significant expression patterns between control and LNP-treated groups

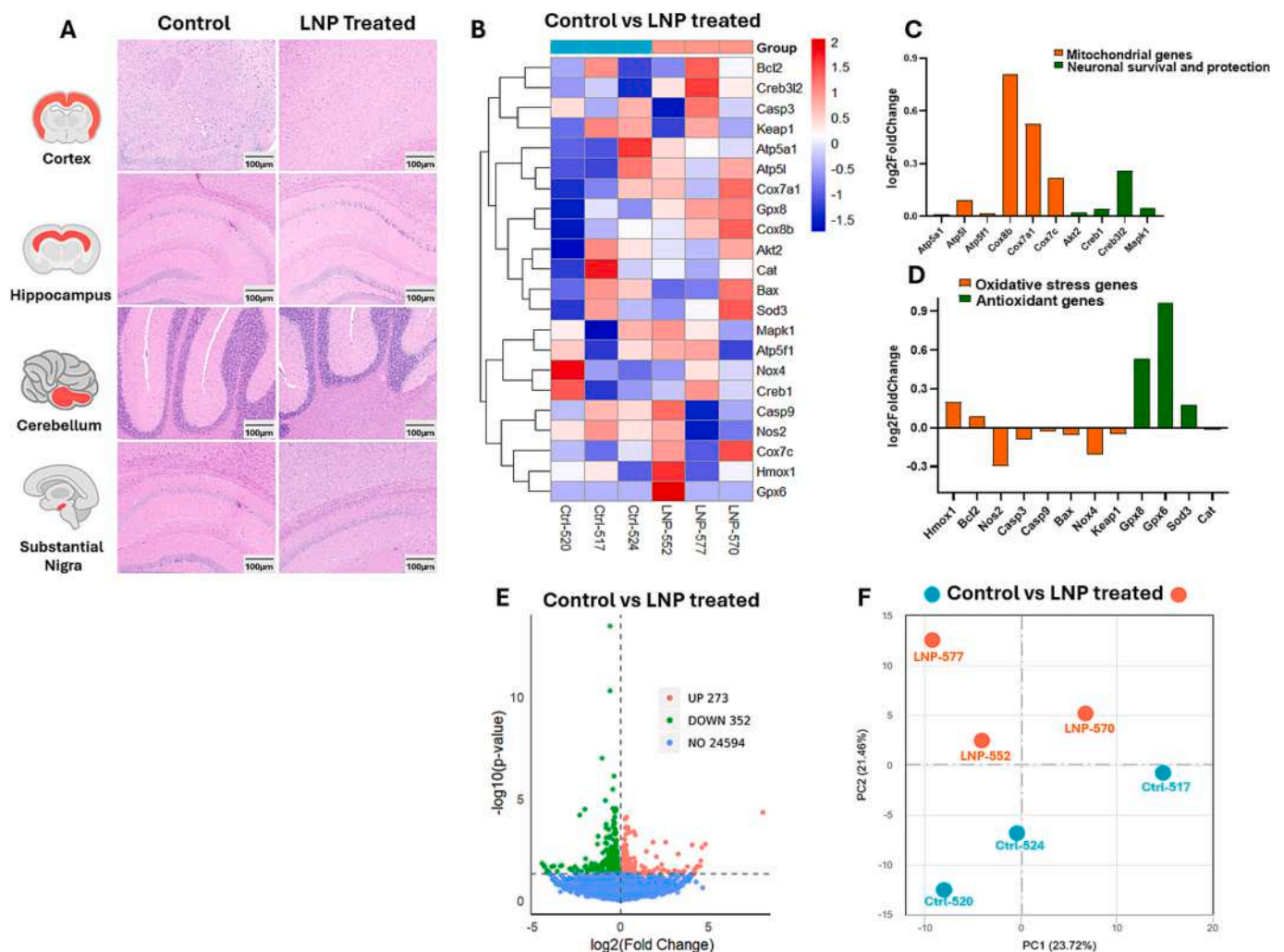


**Fig. 8.** Histological and transcriptomic profiling of mouse brain tissue following treatment with PUFA-GB-Quer-loaded LNPs. (A) Representative H&E-stained brain sections from the cortex, hippocampus, cerebellum, and substantia nigra of PBS-treated control and PUFA-GB-Quer nanoparticle (LNP)-treated C57BL/6J mice after 21 days (once weekly for a total of three doses) of intranasal administration. Both groups exhibit preserved tissue architecture and no visible signs of neuroinflammation, necrosis, or structural damage. (B) Heatmap of selected differentially expressed genes associated with oxidative stress, mitochondrial function, and neuronal survival pathways. (C, D) Bar graph showing log<sub>2</sub>FC in mitochondrial, neuroprotective genes, oxidative stress-related, and antioxidant genes between groups. (E) Volcano plot showing the differential gene expression between control and LNP-treated brain samples. A total of 625 genes were differentially expressed (adjusted  $p < 0.05$ ), with 273 upregulated and 352 downregulated in the LNP-treated group. In the dataset, 24,594 genes showed no significant change. (F) Principal Component Analysis (PCA) reveals partial separation between control (Ctrl-520, Ctrl-524, Ctrl-517) and LNP-treated (LNP-552, LNP-570, LNP-577) groups, with PC1 and PC2 accounting for 23.72 % and 21.46 % of the variance, respectively.

(Fig. 8B). LNP treatment upregulated mitochondria-related genes (*Atp5l*, *Cox8b*, *Cox7a1*, *Cox7c*), neuroprotective markers of synaptic plasticity and resistance to neurodegenerative damage (*Creb1*, *Creb3l2*, *Akt2*, *Mapk1*), and antioxidant genes (*Gpx8*, *Gpx6*, *Sod3*), while pro-oxidative and apoptotic genes (*Casp3*, *Casp9*, *Nos2*, *Bax*) were suppressed (Fig. 7C and D). Considering that the key pro-oxidative and pro-apoptotic genes (*Bax*, *Nos2*, *Casp3*, *Casp9*, *Nox4*) were significantly suppressed (Fig. 8C, D), the results obtained from the *in vivo* study imply that the PUFA-GB-Quer LNPs enhance mitochondrial function by inhibiting oxidative and inflammatory stress in the brain to promote neuronal survival and plasticity.

The focused heatmap analysis revealed a striking upregulation of genes critical for mitochondrial function (*Atp5l*, *Cox8b*, *Cox7a1*, *Cox7c*), antioxidant defense (*Gpx8*, *Gpx6*, *Sod3*), and neuronal survival/plasticity (*Creb1*, *Creb3l2*, *Akt2*, *Mapk1*) (Fig. 8B). These widespread and beneficial gene expression changes strongly indicate that the intranasally delivered PUFA-LNPs effectively engage neuroprotective and mitochondrial-supportive pathways within the brain, consistent with the efficient intracellular delivery facilitated by their pH-responsive structural design.

### 3. Discussion

In the present work, the physicochemical properties of the lipid nanocarriers were rationally designed to respond to biological cues at the mucosal interface relevant to nasal drug delivery. By utilizing the intrinsic ionizability and bioactivity of  $\omega$ -3 PUFAs (EPA and DHA) as integral structural components, alongside monoolein and co-encapsulated antioxidants ginkgolide B (GB) and quercetin (Quer), and functionalizing the PUFA-LNPs with cell-penetrating PACAP for

noninvasive *in vivo* drug delivery to the CNS, we achieved an advanced design of stimuli-responsive nanocarriers for neurological applications.

#### 3.1. Role of Lipid Nanoparticle Topology and Shape for Efficient Nose-to-Brain Delivery

The topology and shape of lipid nanoparticles (LNPs) play a critical role in their interaction with biological membrane barriers, as illustrated in Fig. 2D. Hexosome-type drug delivery nanocarriers exhibit anisotropic geometries, involving elongated, rod-like, or spindle-shaped morphologies, which are particularly favorable for local intranasal drug delivery. The anisotropy arises not from simple cylindrical particles, as typically described in classical SAXS models (e.g., spheres, cylinders, discs), but from an ordered array of densely packed lipid tubes within the internal hexagonal lattice (Figs. 1 and 2). The interfacial and structural characteristics of our ionizable, pH-responsive lyotropic liquid crystalline nanocarriers are essential for achieving efficient drug transport and therapeutic concentrations at the target site. These characteristics directly affect the release kinetics and intracellular uptake of encapsulated therapeutics by regulating the dynamic interactions between the nanocarriers and mucosal interfaces. Furthermore, anisotropic shapes derived from nonlamellar amphiphilic compositions, like lipid/peptide nanoassemblies, may facilitate penetration through the nasal epithelium by promoting stronger adhesion and prolonged residence time. Overall, these structural features of the hexosomes help the nose-to-brain delivery of bioactive compounds.

Towards a more detailed analysis, Fig. 9 presents a typical SAXS curve of hexosome nanoparticles dispersed in solution, along with the corresponding Porod plot. Porod's law describes the asymptotic behaviour of the scattering intensity  $I(q)$  at intermediate values of the

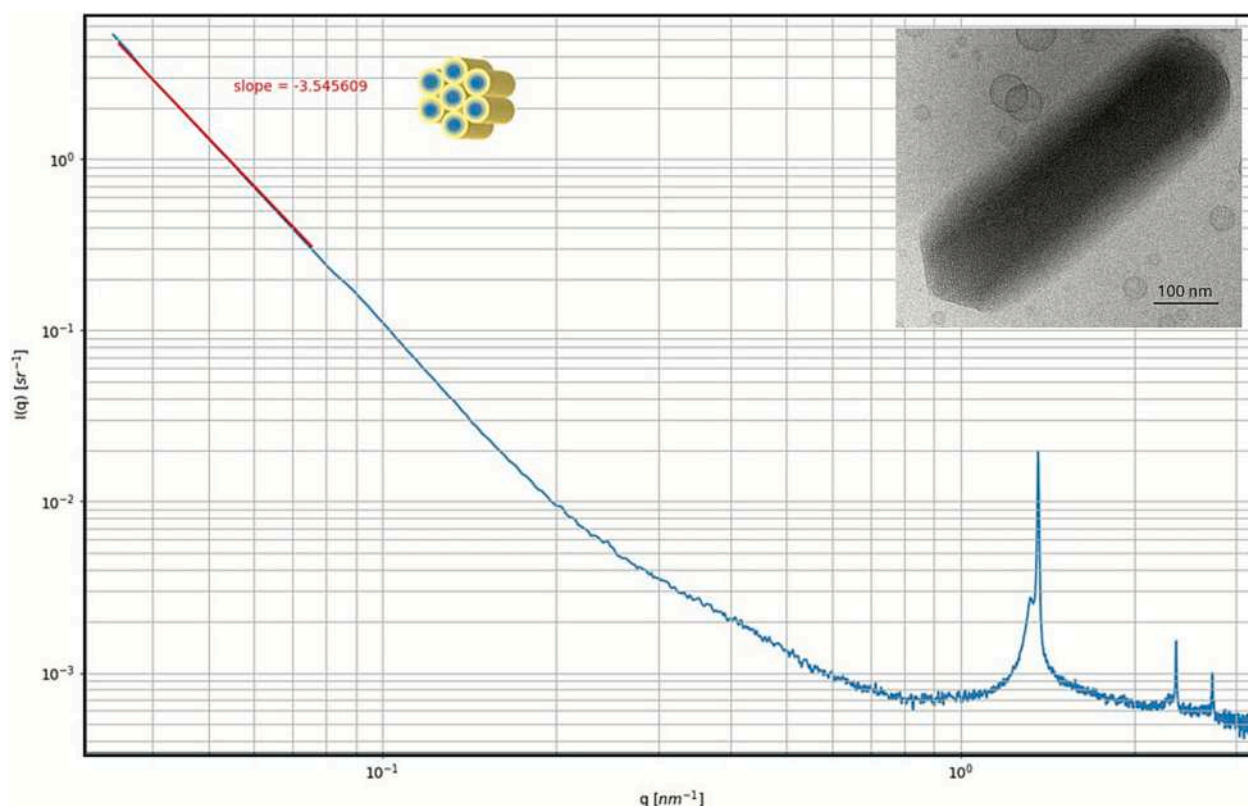


**Fig. 9.** Porod asymptotic regime in the SAXS profile of anisotropic nano-objects, consisting of hexagonal ( $H_{II}$ )-packing of tubes, and dispersed in solution. The insets on the figure show a section of a hexagonal packing of lipid cylinders (left) and a Cryo-TEM image of a hexosome-type lipid nanoparticle (right). The inner liquid crystalline  $H_{II}$ -phase structure is characterized by Bragg peaks at high  $q$ -values. The red line on the scattering function (log-log plot of scattering intensity  $I(q)$  versus scattering vector  $q$ ) represents a Porod asymptotic with a slope of  $-3.5$  that is indicative of flexible, non-sharp interfaces of the hexosomes. (For interpretation of the references to colour in this figure legend, the reader is referred to the web version of this article.)



scattering vector  $q$ ,

$$I(q) \propto q^{-P},$$

where  $I(q)$  is the scattering intensity,  $q$  is the magnitude of the scattering vector, and  $P$  is the Porod exponent, typically ranging from 1 to 4 depending on the investigated structure.

The scattering profile in Fig. 9 reveals a Porod asymptotic behaviour (red line), from which a Porod exponent ( $P$ ) of approximately  $-3.5$  was determined. For compact, smooth-surface particles,  $P \approx 4$ . A Porod slope of  $P \approx 3.5$  suggests deviations from ideal compactness and a fractal character. This slope indicates the formation of a dispersed system with intermediate compactness and flexible interfacial characteristics, which is consistent with the presence of anisotropically shaped particles with large, exposed surfaces. Considering that the surface of the hexosome lipid particles is stabilized by Pluronic copolymer chains (Fig. 1), it can be assumed that these chains impart flexibility to the interface. In addition, the hexosomes are functionalized with polypeptide chains (PACAP) to enable targeted delivery. Despite their densely packed 2D hexagonal liquid-crystalline core (lattice spacing  $\sim 6.05$  nm), the mixed amphiphilic composition of the nanocarriers contributes to a soft nanostructured system with notable surface roughness (often described as “hairy” particles). The performed biological evaluations suggest that the flexible interfacial architecture, the anisotropic shape, and the pH-sensitive  $H_{II}$  internal structure of the hexosomes all play a crucial role in facilitating efficient nose-to-brain drug delivery.

### 3.2. Towards Structural Nanomedicine Development Using PUFAs as Intrinsic Modulators of pH-Responsive Structural Dynamics

Our work demonstrated the purposeful utilization of naturally occurring, bioactive  $\omega$ -3 PUFAs, not merely as therapeutic agents or simple helper lipids (facilitating the encapsulation of hydrophobic antioxidants) but as the primary modulators for the pH-responsive behaviour of the designed LNPs. This contrasts with many conventional LNP designs that rely on synthetic ionizable lipids or complex anchored moieties to achieve stimuli-responsiveness [1,6,8]. Our PUFA-LNPs exploit the inherent acidity of DHA and EPA ( $pK_a \sim 4.6$ – $4.8$ ), allowing their charge state to be modulated by the pH drop in the endosomes (from  $\sim 7.4$  to  $\sim 5.0$ ). This protonation event is hypothesized to alter lipid packing and interfacial curvature, driving structural transformations [38]. It should be noted that the multiple double bonds in DHA and EPA make them more prone to ionization in the biological environment as compared to other fatty acids. Unlike the  $pK_a$  in bulk solution (which is around 4.8 for several carboxylic acids), the  $pK_a$  at a lipid-water interface is significantly higher and often ranges from 6.5 to over 8.0 [39]. E.g., the apparent  $pK_a$  value of oleic acid in DPPC-oleic acid (7:3 mixed) membranes has been estimated to be  $pK_a = 9.4 \pm 0.2$ , whereas the apparent  $pK_a$  for oleic acid in pure oleic acid vesicles has been in the range 8.0–9.5 [40,41].

The *in situ* time-resolved synchrotron SAXS (TR-SAXS) experiments provided direct, millisecond-timescale evidence of these rapid structural reorganizations. Upon exposure to acidic conditions (pH  $\sim 5$ ), the MO-DHA-Plu-GB-Quer LNPs, initially forming an inverted hexagonal ( $H_{II}$ ) phase (with a lattice parameter  $a_{H_{II}} = 6.14$  nm), underwent a dynamic evolution. This involved a rapid shrinkage of the hexagonal lattice (to  $a_{H_{II}} \approx 5.73$  nm and 5.57 nm) and the formation of distinct coexisting  $H_{II}$  domains within 200 ms. Such inverted  $H_{II}$  phases are known for their fusogenic properties and ability to promote membrane destabilization. The pH-triggered shift can be a rate-limiting step in nanoparticle-mediated drug delivery [36,38]. The observed splitting of Bragg peaks under acidic conditions suggested a sophisticated structural reorganization into distinct sub-populations tailored to the acidic trigger. The performed real-time structural characterization offered a significant advantage over studies that infer LNP behaviour or rely on static analyses.

### 3.3. Linking Rapid Structural Changes to Enhanced Neuroprotection and Mitochondrial Integrity

Considering that the release of the hydrophobic antioxidant (Quer) from LNPs is negligible ( $<5\%$ ) at physiological pH 7.4, the purpose of the biological experiments was to establish whether the pH-responsive structural transition of PUFA-LNPs under acidic conditions facilitated the active payloads' release in the microenvironment, thereby enhancing intracellular bioavailability and driving the observed improvements in neuronal outcomes. In SH-SY5Y cells subjected to KPS-induced oxidative stress, treatment with PUFA-LNPs, particularly DHA-formulations, led to notable improvements in neuronal morphology, characterized by extensive, branched neurite outgrowth. This was accompanied by a significant upregulation of tyrosine hydroxylase (TH), a key neurospecific enzyme in catecholamine biosynthesis, suggesting an alleviation of ROS-induced TH downregulation (as observed in Fig. 5F). Quercetin is known for its potentiating action on TrkB receptors, activating ERK and PI3K/AKT pathways [31,32,42]. The potential of GB to increase dopaminergic transmission likely contributes to the established morphological and neurochemical improvements [43].

Furthermore, the investigated LNPs effectively mitigated ROS production and notably enhanced mitochondrial membrane potential ( $\Delta\Psi_m$ ) compared to free ginkgolide B (Fig. S2A and S2B). The restoration of mitochondrial activity is crucial, as mitochondrial dysfunction is a hallmark of oxidative stress-related neurodegeneration [44]. The increased  $\Delta\Psi_m$  directly correlated with increased ATP synthase (Complex V) activity and expression (Fig. 6C,D), and enhanced glutathione peroxidase (GSH-Px) activity (Fig. 6E). This indicates that the PUFA-LNPs not only deliver antioxidants but also actively support the restoration of mitochondrial bioenergetics and cellular redox homeostasis. The ability of EPA/DHA nanoformulations to enhance mitochondrial activity beyond blank-LNPs (vs. KPS controls) evidenced the synergistic benefit of the PUFA-antioxidant cargo combination.

### 3.4. Synergistic Therapeutic Actions of the Bioactive Constituents of the LNPs

The therapeutic efficacy of our PUFA-LNPs stems from a multifaceted approach. The PUFAs themselves (EPA and DHA) are recognized for potent anti-inflammatory, antioxidant, and neuroprotective bioactivities [7,9,23]. DHA, for instance, improves mitochondrial  $Ca^{2+}$  flux and reduces pro-inflammatory cytokines, while EPA can enhance mitochondrial antioxidant enzymes like SOD and GSH-Px [26–30]. Co-encapsulating GB and Quer, known for their mitochondrial protective and antioxidant roles [35,43,45–52], within the bioactive, stimuli-responsive nanocarriers amplifies the therapeutic outcome. Thus, the LNPs ensure coordinated delivery and pH-triggered release of these agents, maximizing their synergistic potential at the target site.

Interestingly, our *in vitro* results suggest that different PUFA-LNP formulations may influence distinct neuroprotective signaling pathways. E.g., MO-EPA-Plu-GB-Quer LNPs induced a more pronounced phosphorylation of ERK and CREB, while MO-DHA-Plu-GB-Quer LNPs showed a stronger impact on p-AKT and BDNF expression (Fig. 7A–D). This lipid-specific modulation opens avenues for fine-tuning therapeutic responses in neuroprotection. The observed mitochondrial HK2 upregulation (Fig. 7E) also points to a role in mitochondrial biogenesis and anti-apoptotic signaling (potentially *via* stabilization at mitochondria-associated membranes (MAMs) and prevention of  $Ca^{2+}$  overload as well as regulation  $Ca^{2+}$  and  $K^+$  flux) [53–55]. The ionic homeostasis stabilization could enhance  $\Delta\Psi_m$ , support ATP synthase function, and consequently impact downstream ERK/CREB signaling.

The surface functionalization with PACAP, a neuropeptide with established neurotrophic effects, further enhanced the neuronal targeting *via* receptor-mediated uptake (PAC1 GPCR), facilitating efficient internalization, as shown by the performed uptake studies (Fig. 6A, B).

PACAP-functionalized LNPs significantly reduced mitochondrial superoxide ( $\text{mitoO}_2^{\bullet-}$ ) by  $\sim 40\%$  (Fig. S2) and restored mitochondrial membrane potential under oxidative stress conditions. These effects exceeded those achieved with the blank MO-Plu carriers or PACAP alone, which shows that the peptide enhances targeted delivery to amplify the antioxidant impact of the GB + Quer payload rather than direct mitochondrial modulation (Figs. S1 and S2B).

### 3.5. In Vivo Evidence of Biocompatibility and Neuroprotective Gene Expression

The *in vivo* studies involving intranasal administration of PACAP-functionalized MO-EPA-Plu-GB-Quer LNPs in C57BL/6 J mice provided a crucial safety evaluation. Histological analyses of major brain regions revealed preserved tissue architecture, with no signs of inflammation or tissue damage, and demonstrated the excellent biocompatibility of the LNPs (Fig. 8A). This is a critical characteristic for any CNS therapeutic, especially for chronic administration.

More importantly, transcriptomic profiling of brain tissue via RNA-Seq unveiled a profound neuroprotective gene expression signature (Fig. 8B-F). LNP treatment led to a significant upregulation of genes critical for mitochondrial function (e.g., *Atp5l*, *Cox8b*, *Cox7a1*, *Cox7c*), antioxidant defense (e.g., *Gpx8*, *Gpx6*, *Sod3*), and neuronal survival/plasticity (e.g., *Creb1*, *Creb3l2*, *Akt2*, *Mapk1*) (Fig. 8C). Concurrently, key pro-oxidative and pro-apoptotic genes (e.g., *Casp3*, *Casp9*, *Nos2*, *Bax*) were significantly suppressed (Fig. 8D). These beneficial gene expression changes strongly indicate that the intranasally delivered PUFA-LNPs may positively impact neuroprotective and mitochondrial-supportive pathways within the brain.

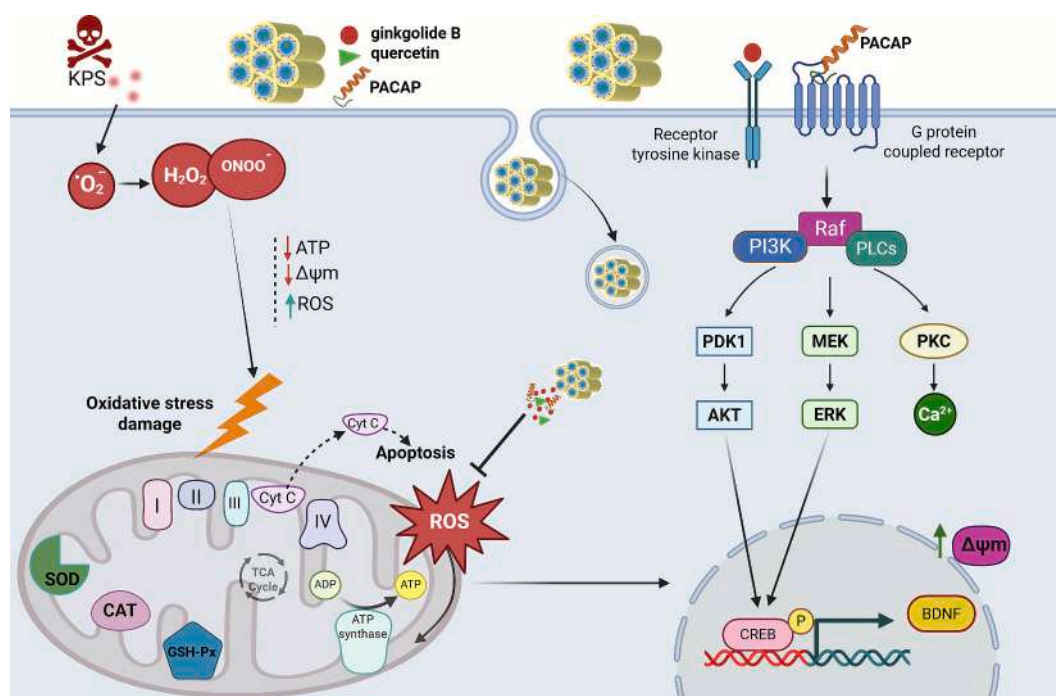
### 3.6. A Mechanistic Hypothesis about Lipid-Peptide Nanoassembly-Driven Regulation of Mitochondrial and Antioxidant Pathways

Fig. 10 presents our hypothesis for the nanomedicine-mediated regulation of mitochondrial protein function and antioxidant enzyme activity by the designed PUFA lipid-peptide (PACAP) liquid crystalline nanoassemblies in an *in vitro* oxidative stress model. Exposure to oxidative agent (KPS) induces excessive ROS production, leading to oxidative stress, mitochondrial dysfunction (characterized by electron transport chain damage, ATP depletion, and cytochrome *c* release), and downregulation of glutathione peroxidase activity, potentially promoting apoptosis. This can inhibit crucial survival signaling pathways like ERK, AKT, or PKC, resulting in CREB downregulation.

Our PUFA-LNPs, co-encapsulating GB and Quer and functionalized with PACAP, regulated this signaling cascade. The pH-triggered release of GB and Quer allows them to neutralize ROS. The LNPs can activate CREB signaling and BDNF release via Ras-Raf-MEK-ERK or PI3K-AKT pathways. CREB can also be phosphorylated via PKC-Calcium activation, mediated by G-protein-coupled receptors (like PAC1 for PACAP) or receptor tyrosine kinases. This multifaceted activation aims to restore cellular homeostasis.

## 4. Conclusion

In this study, we investigated how the structural and interfacial properties of designed ionizable, pH-responsive lipid-peptide nanoassemblies based on  $\omega$ -3 polyunsaturated fatty acids (EPA and DHA), monoolein, and multifunctional bioactives (ginkgolide B and quercetin), further functionalized with PACAP for targeted neuronal delivery, determine their biological effects. The hexosomal liquid crystalline nanoparticles (PUFA-LNPs) were engineered to address the challenges of



**Fig. 10.** Drug delivery by ionizable PUFA, synergistically functionalized hexosomal lipid-peptide nanoassemblies in an *in vitro* oxidative stress model relevant to neurological disorders and hypothesized regulation of mitochondrial proteins (APT synthase and HK2) and mitochondrial antioxidant enzyme function. Excessive ROS production triggers oxidative stress that causes mitochondrial dysfunction, mitochondrial electron transport chain damage, ATP depletion, and cytochrome *c* release and downregulation of glutathione peroxidase activity, which may promote apoptosis. An *in vitro* oxidative stress model was established by differentiation of SH-SY5Y cells using retinoic acid (RA) for 5 days and subsequent acute exposure to KPS for 30 min, which resulted in mitochondrial dysfunction, apoptosis, and inhibition of ERK, AKT, or PKC, leading to the downregulation of CREB. PUFA-LNPs, encapsulating neuroprotective molecules such as GB, Quer, and the neurotrophic peptide PACAP, may activate the CREB signaling pathway and favor the release of BDNF via Ras-Raf-MEK-ERK or PI3K-AKT signaling cascades. CREB transcription factor can also be phosphorylated by activation of the PKC-Calcium pathway through a receptor-mediated mechanism such as a G-protein-coupled receptor or a receptor tyrosine kinase.

noninvasive nose-to-brain delivery by combining structural adaptability, bioactivity, and targeting specificity.

The results obtained suggest that the anisotropic shape, the pH-sensitive  $H_{II}$  internal structure of the PUFA lipid hexosomes, and their flexible interfacial architecture all play a crucial role in facilitating efficient nose-to-brain drug delivery. Our key findings reveal that the PUFA-LNPs undergo a rapid, pH-triggered structural change of the hexagonal liquid crystalline assemblies, enabling efficient cytosolic delivery of hydrophobic therapeutic cargos. Time-resolved SAXS studies confirmed the dynamic reorganization of the PUFA-LNPs under acidic conditions. Importantly, the co-encapsulated antioxidants provided synergistic mitochondrial protection, as evidenced by enhanced activity of ATP synthase, HK2, and GSH-Px, alongside favorable modulation of neuroprotective signaling pathways (AKT/ERK/CREB/BDNF) in oxidative stress-challenged neuronal cells.

Compared to existing literature, our approach introduces several novelties: (i) Strategic use of ionizable PUFAs not only as therapeutic agents but as structural building blocks of stimuli-responsive behaviour; (ii) Synergistic multi-functionalization with natural antioxidants and PACAP for enhanced neuroprotection and targeting; (iii) Lyotropic hexosomal architectures offering superior intracellular release dynamics tailored for neuronal therapies; (iv) *In vivo* validation via intranasal administration in C57BL/6 J mice, showing safety and transcriptomic evidence of mitochondrial and antioxidant pathway activation without inflammation or toxicity.

Looking ahead, these advances position our PUFA-LNP platform as a next-generation nanomedicine strategy for treating neurodegenerative and oxidative stress-related disorders. By rationally exploiting the intrinsic chemical and self-assembly properties of lyotropic lipids, we propose a multifaceted solution to overcome biological barriers and enhance therapeutic efficacy.

## 5. Experimental section

### 5.1. Materials

The  $\omega$ -3 polyunsaturated fatty acids (PUFA) cis-4,7,10,13,16,19-Docosahexaenoic acid (DHA) and cis-5,8,11,14,17-Eicosapentaenoic acid (EPA) were purchased from Sigma-Aldrich (purity >99 %). The fluorescent lipid 1,2-dioleoyl-sn-glycero-3-phosphoethanolamine-N-(lissamine rhodamine B sulfonyl) (ammonium salt) (18:1 Liss Rhod PE) was purchased from Avanti Polar Lipids, Inc. (Alabama). Monoolein (MO, C18:1c9, powder, ≥99 %), retinoic acid (RA), Ginkgolide B (GB), quercetin (Quer), 2,6-di-tertbutyl-4-methylphenol (BHT), and FCCP (carbonyl cyanide 4-(trifluoromethoxy)phenylhydrazone) were purchased from Sigma-Aldrich. The peptide PACAP (MW 4535 Da, purity 99.48 %) and the fluorescent conjugate of PACAP with tetramethylrhodamine PACAP-TAMRA (MW 4948 Da, purity 95.97 %) were custom synthesized by QYAOBIO (China Peptides Co., Ltd., Rep. China). Water of MilliQ quality (Millipore Corp., Molsheim, France) was used for preparation of a phosphate buffer solution ( $\text{NaH}_2\text{PO}_4/\text{Na}_2\text{HPO}_4$ ,  $1 \times 10^{-2}$  M, pH 7, p.a. grade, Merck).

### 5.2. Lipid Nanoparticle Formulation

Lyotropic liquid crystalline nanoparticles were prepared using the method of hydration of a lyophilized thin lipid film, followed by physical agitation in an aqueous phase [54–56]. The formulations, including MO-Plu (90:10), MO-EPA-Plu-GB-Quer (80:20:10:7:2), and MO-DHA-Plu-GB-Quer (80:20:10:7:2) wt%, comprised of monoolein, EPA, DHA, and Pluronic F127. The lipids, surfactants, and active compounds were first dissolved in chloroform. The chloroform was then evaporated under a nitrogen gas stream at room temperature for 1 h, resulting in the formation of a thin lipid film. To remove any residual organic solvent, the samples were lyophilized overnight under cooling. The lipid films were subsequently hydrated at room temperature in a  $1 \times 10^{-2}$  M phosphate

buffer (pH 7.4) containing 2,6-di-tertbutyl-4-methylphenol and prepared with Milli-Q water. The phosphate buffer with BHT was purged with nitrogen gas to eliminate dissolved oxygen and then filtered through a 0.2  $\mu\text{m}$  sterile filter (Millipore Corp.) [34,56].

### 5.3. Static Synchrotron Small-Angle X-ray Scattering (SAXS) Characterization

For static SAXS measurements at the SWING beamline of Synchrotron SOLEIL (Saint Aubin, France), the samples were sealed by paraffin wax in X-ray capillaries of a diameter  $\phi = 1.5$  mm. The sample-to-detector distance was 2 m. They were oriented in front of the X-ray beam ( $25 \times 375 \mu\text{m}^2$ ) using a designed holder for multiple capillary positioning (X, Y, and Z). The patterns were recorded with a two-dimensional EigerX 4 M detector (DECTRIS, Ltd.) at 12 keV, allowing measurements in the  $q$ -range from 0.00426 to  $0.37 \text{ \AA}^{-1}$ . The synchrotron radiation wavelength was  $\lambda = 1.033 \text{ \AA}$ . The  $q$ -range calibration was done using a standard sample of silver behenate ( $d = 58.38 \text{ \AA}$ ).

Static SAXS measurements were also performed at the ID02 beamline of the European Synchrotron Radiation Facility (ESRF), Grenoble, France. The experiments utilized an X-ray energy of 12.230 eV ( $\lambda = 1.013 \text{ \AA}$ ) with a photon flux of  $1.18 \times 10^{12}$  photons/s and a camera length of 2 m. The reported range of the scattering vector,  $q = 4\pi\sin\theta/\lambda$ , was approximately  $0.0034\text{--}0.368 \text{ \AA}^{-1}$ , where  $\theta$  is the scattering angle, and  $\lambda$  is the wavelength. The samples were loaded into a Peltier-controlled flow-through capillary cell with a diameter of  $\phi = 2$  mm. The exposure time was 0.1 s, and data were collected using a pixel array detector Eiger2-4 M (DECTRIS). The acquired 2D patterns were normalized to an absolute intensity scale and azimuthally averaged to obtain 1D scattered intensity profiles. The experiments were performed at 22 °C. The SAXS pattern of a background sample, composed of a phosphate buffer (pH 7.4 or pH 5.0), was subtracted from the samples.

The data analysis was performed using the ATSAS 3.3.0 software suite with the PRIMUS feature. The lattice parameters of the liquid crystalline lipid phases were determined by analyzing the Bragg peaks observed in the X-ray diffraction patterns. For cubic phases, the lattice parameter  $a_0$  is determined by the formula  $a_0 = d(h^2 + k^2 + l^2)^{1/2}$ , where the repeat spacing ( $d$ ) is derived from Bragg's law,  $d = 2\pi/q$ . It corresponds to the repeat distance between the scattering planes (i.e.,  $1/d^2 = (h^2 + k^2 + l^2)/a^2$ ) [57]. The resolved Bragg reflections were assigned based on the Miller indices ( $hkl$ ). For structures with a lamellar spacing, the relationship is expressed as  $a/d = 1, 2, 3, \dots$

For cubic structures of the primitive (P) type ( $Im\bar{3}m$  space group), the relationship follows the sequence  $(a/d)^2 = 2, 4, 6, 8, 10, 12, 14, 16, 18, 20, 22, \dots$

For hexagonal phases, the lattice parameter ( $a_H$ ) is determined using the equation:  $a = d(2/\sqrt{3})(h^2 + k^2 - hk)^{1/2}$  [58].

### 5.4. Time-Resolved SAXS Investigation

The time-resolved SAXS investigation of ionizable PUFA lipid assemblies was performed at the ID02 beamline of ESRF with a stopped-flow rapid mixing device (SFM-4000; Biologic). For acidification experiments, PUFA-LNP dispersion was rapidly mixed with pH 2.8 phosphate buffer at a mixing ratio of 1.1 (v/v) by the stopped-flow rapid mixing device, resulting in a final pH of 5.0. During the *in-situ* kinetic process, the samples were exposed to synchrotron X-ray radiation (photon flux of  $1.3 \times 10^{13}$  photons/s) using a flow-through cell ( $\phi = 1.3$  mm) for an exposure time of 5 ms. To minimize radiation-induced damage, frames were recorded at intervals following a geometrical progression, optimizing data collection while reducing prolonged exposure. For the acquisition sequence, an initial "dead time" was introduced and adjusted to ensure that the first frame was acquired towards the end of the mixing process. Each kinetic experiment was repeated at least four times, and a representative scan was selected for analysis [59,60].



### 5.5. Lipid peroxidation (MDA Assay)

Lipid peroxidation was quantified by measuring malondialdehyde (MDA), a stable end-product of lipid peroxidation, using the MDA Assay Kit (Colorimetric, ab233471, Abcam, UK). For the assay, 50  $\mu\text{L}$  of standards or PUFA-LNPs were loaded into a 96-well clear-bottom microplate, followed by the addition of 10  $\mu\text{L}$  MDA Colour Reagent. After incubation at room temperature for 30 min in the dark, 40  $\mu\text{L}$  of Reaction Solution was added to each well, and the mixture was incubated for an additional 60 min at room temperature. Absorbance was measured at 600 nm using a microplate reader. All samples and standards were assayed in duplicate.

### 5.6. In Vitro Release Studies

Chromatographic analyses were performed using a Waters UPLC system (Waters Corporation, Singapore) equipped with a photodiode array (PDA e $\lambda$ ) detector. Separation was achieved on a ZORBAX Eclipse Plus C18 column (100 mm  $\times$  4.6 mm, 3.5  $\mu\text{m}$ ; Agilent, part no. 959961–902). The mobile phase consisted of 0.1 % formic acid in water (solvent A) and methanol (solvent B) and was delivered at a flow rate of 0.7 mL min<sup>−1</sup> under a step gradient elution. The column temperature was maintained at 30 °C, and UV detection was performed at 371 nm. *In vitro* drug release was assessed using Slide-A-Lyzer® MINI Dialysis Devices (Prod# 88401) with a molecular weight cut-off (MWCO) of 10 kDa. A total of 300  $\mu\text{L}$  of the LNP dispersion was loaded into the mini dialysis device and immersed in 14 mL of release medium buffer, adjusted to either pH 5.0 or pH 7.4. Aliquots of the release medium were withdrawn at 1, 2, 3, 4, and 24 h, diluted with 1 mL of 50:50 methanol/water, filtered through a 0.22  $\mu\text{m}$  membrane, and 20  $\mu\text{L}$  of the filtrate was injected into the UPLC system for quantification. Data analysis was performed using Waters MassLynx™ software.

### 5.7. Cell Culture

The human neuroblastoma SH-SY5Y cells were cultured in Dulbecco's Modified Eagle's Medium (DMEM, Sigma, France), supplemented with 1 % penicillin-streptomycin (Sigma) and 10 % (v/v) fetal bovine serum (FBS, Sigma). The cells were maintained in a humidified incubator with 5 % CO<sub>2</sub> at 37 °C and subcultured every three days. The cells were first washed with sterile, calcium-free phosphate buffered saline (PBS) and detached by incubation with 3 mL of trypsin (0.05 % w/v)/EDTA (0.02 % w/v) for 5 min. The reaction was stopped by adding 7 mL of fresh DMEM complete medium. The cell suspension was centrifuged at 200 g for 5 min at 4 °C, and the pellet was resuspended in 10 mL of fresh complete medium. For experiments, SH-SY5Y cells were differentiated into a neuronal phenotype using 10  $\mu\text{M}$  retinoic acid (RA) for five days. Differentiation was initiated when the cells reached 70–80 % confluency, typically on the second day after seeding, by substituting the medium with 15 mL of fresh complete medium containing 10  $\mu\text{M}$  RA.

### 5.8. Cell Viability Assay

The SH-SY5Y cells ( $1 \times 10^4$  cells/well) were seeded into 96-well plates and incubated overnight at 37 °C in a 5 % CO<sub>2</sub> atmosphere to allow for adhesion. The culture medium was replaced with a fresh complete medium supplemented with 10  $\mu\text{M}$  retinoic acid (RA), and the cells were cultured for five days, during which differentiation was regularly observed under the microscope. The cells were treated with varied concentrations of nanoparticles (1–300  $\mu\text{M}$ ) for 24 h. The control cells, referred to as RA/FBS(–), correspond to RA-differentiated cells deprived of FBS for 24 h. Following treatment, the medium was removed, and 20  $\mu\text{L}$  of MTT reagent (3-(4,5-dimethylthiazol-2-yl)-2,5-diphenyltetrazolium bromide) was added at a concentration of 5 mg/mL to each well. The cells were incubated for 1 h to allow the formation of formazan crystals. Afterwards, the medium was discarded, and the

formazan crystals were dissolved in DMSO. The absorbance at 570 nm was measured using a spectrophotometer (LT-5000 MS, Labtech) to assess cell viability. The MTT solution was prepared in PBS, filtered, and used immediately for the assay.

### 5.9. Cellular Uptake of Nanoparticulate Assemblies

SH-SY5Y cells were seeded in 6-well plates at a density of  $3 \times 10^5$  cells per well and differentiated over 5 days with 10  $\mu\text{M}$  RA. The medium was replaced with fresh RA/FBS(–) medium containing fluorescently-labeled nanoassemblies and incubated for various time intervals. The cells were washed three times with cold PBS, detached using an appropriate buffer, and centrifuged at 200 g for 5 min. The resulting cell pellet was resuspended in 1 mL PBS, and the fluorescence intensity was analyzed using a flow cytometer (BD Accuri C6), with readings recorded in the FL2 and FL3 channels for Rhod-LNP and TAMRA-LNP, respectively.

### 5.10. Quantification of Phosphorylated CREB, AKT, and ERK Proteins Using ELISA

Phosphorylated ERK1/ERK2 and phosphorylated AKT levels in cell lysates from lipid nanoparticle-treated samples were measured using the respective ELISA kits: Phospho-ERK1/2 DuoSet™ IC ELISA (Catalog #DYC1018B-5) and Phospho-AKT Pan Specific DuoSet® IC ELISA (Catalog #DYC887B-5, Bio-Techne Ltd./R&D Systems, UK). The kits are designed to specifically detect AKT and ERK1/2 phosphorylation at Threonine/Tyrosine (T202/Y204/ T185/Y187) phosphorylation sites on the amino acid sequence and Serine 473, respectively, in cell lysate. Phosphorylated CREB (p-CREB) was also quantified using the Phospho-CREB DuoSet® IC ELISA kit (Catalog #DYC2510–5, Bio-Techne Ltd./R&D Systems, UK), which is designed to detect phosphorylation at Serine 133 specifically. Cell lysates were prepared using a specialized lysis buffer, and the assays were performed according to the protocols provided with the DuoSet® ELISA ancillary reagent kits (Catalog #DY008, Bio-Techne Ltd./R&D Systems, UK). The 96-well plates were pre-coated with monoclonal antibodies specific to p-CREB, p-AKT, or p-ERK1/2. Protein standards and cell lysates were added to the wells and incubated for 2 h, allowing the target proteins to bind to the immobilized antibodies. Afterwards, an enzyme-linked monoclonal antibody specific to the target protein was added and incubated for 1 h at room temperature. Following three washes with the provided buffer, a substrate solution was added to facilitate colour development. The colour intensity, which was proportional to the protein levels, was measured using a plate reader at 450 nm within 30 min of stopping the reaction with a stop solution. This process enabled the quantification of phosphorylated CREB, AKT, and ERK proteins.

### 5.11. Quantification of Human BDNF Using ELISA Immunoassay

Human-free BDNF levels were assessed following a 48-h treatment with lipid nanoparticles after exposure of SH-SY5Y cells to KPS for 30 min. The quantification was performed using the Human Free BDNF Immunoassay ELISA kit (Catalog #DBD00, R&D Systems, Bio-Techne Ltd., UK). The 96-well microplate, pre-coated with a monoclonal antibody specific for human-free BDNF, was loaded with 50  $\mu\text{L}$  of standards, controls, or samples, along with 100  $\mu\text{L}$  of Assay Diluent, and incubated for 2 h at room temperature. After incubation, 100  $\mu\text{L}$  of enzyme-linked monoclonal antibody specific for human BDNF was added, and the plate was incubated for an additional hour. Following three washes with the provided wash buffer to remove unbound reagent, 200  $\mu\text{L}$  of substrate solution was added to each well, and the plate was incubated for 30 min at room temperature, protected from light. The reaction was stopped by adding 50  $\mu\text{L}$  of stop solution, resulting in a colour change from blue to yellow. The absorbance was measured using a microplate reader at 450 nm within 30 min of stopping the reaction.

### 5.12. Quantification of Mitochondrial-Associated Proteins ATP Synthase (Complex V) and Hexokinase 2 (HK2)

The levels of ATP synthase (Complex V) and Hexokinase 2 (HK2) in cell lysates were measured using the respective ELISA kits: ATP Synthase Human Profiling ELISA Kit (Catalog #ab124539, Abcam, UK) and human HK2 (Catalog #KA6013, Abnova). Samples, controls, and standards were diluted in incubation buffer, and 50  $\mu$ L was added to each well, followed by a 2-h incubation at room temperature. After washing, 50  $\mu$ L of either ATP synthase Detector Antibody or Biotinylated Human Hexokinase-2 antibody was added and incubated for an additional hour. Subsequently, for ATP detection, HRP-labeled secondary antibody (50  $\mu$ L) and HRP Development Solution (100  $\mu$ L) were added and incubated for another hour. The colour development was recorded kinetically at 600 nm for 15 min. In parallel, SP Conjugate and Chromogen Substrate (50 + 50  $\mu$ L) were added to the plate corresponding to HK2. The reaction was stopped with 50  $\mu$ L stop solution, and absorbance was read at 450 nm.

### 5.13. Intracellular ROS Detection by Flow Cytometry

Intracellular ROS levels were analyzed using flow cytometry with the non-fluorescent, cell-permeable compound DCFH-DA. DCFH-DA is hydrolyzed by esterases to form DCFH, which is then oxidized by ROS to produce DCF, a fluorescent compound. DCF emits green fluorescence with an excitation wavelength of 488 nm and an emission wavelength of 533 nm, with the fluorescence intensity directly proportional to the ROS concentration. Experiments with KPS (oxidative agent) and LNPs were conducted for cells exposed to 50 mM KPS for 30 min to induce ROS, followed by treatment with 1  $\mu$ M LNPs for 24 h. The cells were incubated with 10  $\mu$ M DCFH-DA in an FBS-free medium for 30 min at 37 °C before analysis. The cells were washed twice and analyzed using flow cytometry (BD Accuri C6).

### 5.14. Mitochondrial Membrane Potential Assay Using JC-10 Dye

The mitochondrial membrane potential was assessed using the JC-10 Assay Kit (Catalog #MAK160, Sigma-Aldrich). SH-SY5Y cells were seeded in 6-well plates at a density of  $3 \times 10^5$  cells per well and differentiated for 5 days using 10  $\mu$ M retinoic acid (RA). After differentiation, the cells were treated with 1  $\mu$ M LNPs for 24 h in a serum-free medium. The mitochondrial uncoupling agent FCCP (5  $\mu$ M) was used as a positive control (inducing mitochondrial depolarization by uncoupling mitochondrial respiration), while RA-differentiated cells in serum-free medium (RA/FBS(-)) served as a negative control. The cells were stained with JC-10 dye for 15 min at 37 °C, protected from light. Following staining, the cells were washed twice with PBS and detached using 0.5 mL trypsin-EDTA. The resulting suspension was transferred to Eppendorf tubes, centrifuged at 200 g for 5 min, and the pellet was washed twice with PBS. The fluorescence intensity was measured using a BD Accuri C6 flow cytometer, recording green fluorescence (FL1) and red fluorescence (FL2). The ratio of red to green fluorescence (FL2/FL1) was calculated to determine mitochondrial polarization.

### 5.15. Tyrosine Hydroxylase (Phospho-Ser31) ELISA Assay

The Tyrosine Hydroxylase (Phospho-Ser31) levels in cultured cells were analyzed using the CytoFluor™ Fluorometric Cell-Based ELISA Kit (Catalog #FLUO-CBP1036, Assay Biotechnology). SH-SY5Y cells were seeded at a density of  $3 \times 10^4$  cells per well in a 96-well black cell culture clear-bottom microplate and incubated overnight at 37 °C with 5 % CO<sub>2</sub>. After treatment, cells were fixed using 4 % formaldehyde for 20 min at room temperature, quenched and blocked with a quenching and blocking Buffer. To detect phosphorylated and non-phosphorylated tyrosine hydroxylase, 50  $\mu$ L of primary antibodies were added, and the plate was incubated overnight at 4 °C. After washing, 50  $\mu$ L of

Secondary Antibody Mixture was added, and the plate was incubated for 1.5 h at room temperature, protected from light. The fluorescence intensities were measured at Ex/Em: 651/667 nm (Dye 1) and 495/521 nm (Dye 2) using a fluorescent plate reader. The obtained RFU values were normalized to GAPDH levels.

### 5.16. Determination of Glutathione Peroxidase (GSH-Px) Enzymatic Activity in SH-SY5Y Cell Lysates

Total GSH-Px concentrations in the cell lysates were measured using a GSH-Px assay kit (Cayman Chemical Co., Catalog #703102, Ann Arbor, MI). The activity of GSH-Px was assessed in differentiated SH-SY5Y cells seeded in 75 cm<sup>2</sup> flasks at a density of  $5 \times 10^6$  cells. The cells were treated with 1  $\mu$ M LNPs after inducing oxidative stress with 50 mM KPS for 30 min. The cells were lysed using CellLytic M mammalian cell lysis buffer (Sigma-Aldrich, Catalog #C2978) and collected by centrifugation at 1500 g for 15 min at 4 °C. GSH-Px activity was determined indirectly through a coupled reaction involving glutathione reductase (GR), hydrogen peroxide (H<sub>2</sub>O<sub>2</sub>) and NADPH. This reaction leads to the oxidation of NADPH to NADP<sup>+</sup>, resulting in a decrease in absorbance at 340 nm. The reduction in absorbance is directly proportional to the enzymatic activity of GSH-Px in the sample. The GSH-Px assay was conducted on the resulting cell lysates according to the kit manufacturer's instructions.

### 5.17. Assessment of Total Protein Concentration

The total protein concentration in cell lysates was determined using the Bradford Protein Assay, conducted in 96-well plates. A stock solution of bovine serum albumin (BSA) at a concentration of 2 mg/mL in PBS was prepared to create a calibration curve with seven BSA standards as references. For each assay, 20  $\mu$ L of either BSA standard or cell lysate sample was added to the wells and mixed with 180  $\mu$ L of Bradford reagent (Sigma, Catalog #B6916-500ML). The absorbance was measured at 595 nm using a microplate reader, and the optical density of a blank well was subtracted from each reading. The protein concentrations of the GSH-Px, TH, phosphorylated AKT, ERK1/2, CREB, and BDNF samples were then normalized by dividing their respective values by the total protein concentration measured in the corresponding samples.

### 5.18. In Vivo Animal Studies

The *in vivo* studies were conducted using the PACAP-functionalized PUFA-LNPs to leverage the nose-to-brain targeting advantage. For safety evaluation, the C57BL/6JGpt strain was used as a standard and widely used background strain, which ensures genetic consistency and comparability with a large body of literature. All animal procedures were approved by the Institutional Animal Care and Use Committee (IACUC) at Wenzhou Institute, University of Chinese Academy of Sciences (Approval No. GJS0420231201118). Male C57BL/6JGpt mice ( $n = 6$ ) were sourced from GemPharmatech Co., Ltd. The study involved 10-week-old male C57BL/6JGpt mice and comprised two main groups ( $n = 3$  each): a WT group and an LNP-treated group. The control group received phosphate-buffered saline (PBS), while the LNP-treated group was administered intranasally with formulation drops. Each mouse received bilateral intranasal drops (20  $\mu$ L per nostril) weekly for three weeks using micropipette equipment.

### 5.19. Histological Analysis of Brain Sections

Brain tissues (hippocampus, frontal cortex, substantia nigra, and cerebellum) were collected from the control and LNP-treated groups ( $n = 3$  mice per group) and processed for hematoxylin and eosin staining. The tissues were dehydrated with a Donatello tissue processor (DIAPATH) and embedded in paraffin using the JB-P5 embedding machine. Brain sections of 5  $\mu$ m were cut with an RM2016 rotary microtome and

mounted onto HDAS001A glass slides. After sectioning, slides were deparaffinized in xylene (Cat. No. 10023418, Sinopharm) and rehydrated through a graded ethanol series (75 %, 85 %, 95 %). Sections were stained with a commercial H&E staining kit (Cat. No. G1120, Solarbio). Microscopic analysis was carried out using a Nikon Eclipse E100 upright fluorescence microscope, and imaging was captured using a Nikon DS-U3 system. The result interpretation was based on standard morphology: nuclei presented in blue and cytoplasm in red, allowing evaluation of tissue architecture and potential pathological changes.

### 5.20. RNA-Seq sequencing sample preparation and analyses

RNA integrity was evaluated using the RNA Nano 6000 Assay Kit of the Agilent 2100 Bioanalyzer (Agilent Technologies, USA). High-quality RNA samples were used for library construction. mRNA was purified using poly-T oligo-attached magnetic beads, fragmented, and reverse transcribed into cDNA. After second-strand synthesis and adaptor ligation, fragments of 370–420 bp were selected with the AMPure XP system (Beckman Coulter), PCR-amplified, and quality-checked using the Bioanalyzer. Libraries were sequenced on an Illumina NovaSeq platform (150 bp paired-end reads) [61,62]. The raw reads were filtered using *fastp*, and clean reads were aligned to the mouse reference genome with HISAT2 (v2.0.5). Transcript assembly was performed with StringTie (v1.3.3b), and gene expression levels were quantified using featureCounts. Differential expression analysis was conducted using DESeq2 or edgeR, depending on replication [63–69]. Genes with  $p \leq 0.05$  were considered significant.

### 5.21. Statistical analysis

Statistical analyses were carried out using GraphPad Prism version 9.5.1, with results expressed as mean  $\pm$  SD. An Independent Student's *t*-test was used for two-group comparisons, while one-way and two-way ANOVA were employed for analyzing multiple groups. *p* values of  $<0.05$  were considered significant. Furthermore, the Sigmoidal 4PL model was utilized to evaluate the relationship between cellular responses and protein expression levels.

### CRediT authorship contribution statement

**Thelma Akanchise:** Writing – review & editing, Writing – original draft, Methodology, Investigation, Formal analysis, Data curation. **Fucen Luo:** Writing – review & editing, Methodology, Investigation, Data curation. **Borislav Angelov:** Writing – review & editing, Validation, Resources, Methodology, Investigation, Funding acquisition, Formal analysis, Data curation. **Yuru Deng:** Writing – review & editing, Validation, Resources, Project administration, Methodology, Investigation. **Gouranga Manna:** Visualization, Software, Methodology, Investigation, Formal analysis, Data curation. **Angelina Angelova:** Writing – review & editing, Supervision, Project administration, Methodology, Investigation, Conceptualization.

### Declaration of competing interest

The authors declare that they have no known competing financial interests or personal relationships that could have appeared to influence the work reported in this paper.

### Acknowledgments

Thelma Akanchise acknowledges a PhD fellowship from Campus France, and Angelina Angelova acknowledges membership in the CNRS GDR2088 BIOMIM research network. The performed research was partially funded by the projects “Structural dynamics of biomolecular systems (ELIBIO)” (No. CZ.02.1.01/0.0/0.0/15\_003/0000447) from the European Regional Development Fund, by the Czech Science

Foundation (GACR project No. 24-10671S), and the PHC Štefanik project 53619ZF. The authors thankfully acknowledge the scientific support by Dr. Thomas Bizien at the SWING beamline of Synchrotron SOLEIL (Saint Aubin, France) and the allocation of beam time through project 20230326. We thank ESRF for the allocation of beamtime for a millisecond time-resolved SAXS study at the ID02 beamline (project SC-5591) and acknowledge interesting discussions with Dr. Theyencheri Narayanan. T.A. thanks Mélanie Hery (Cell culture platform), Lynda Benrabah, and Martin Souce (HPLC platform) for advice or training. Figs. 1 and 10 were generated with *BioRender.com* (accessed on March 6, 2025).

### Appendix A. Supplementary data

Supplementary data to this article can be found online at <https://doi.org/10.1016/j.jcis.2025.139420>.

### Data availability

Data will be made available on request.

### References

- [1] J. Zhai, C. Fong, N. Tran, C.J. Drummond, Non-lamellar lyotropic liquid crystalline lipid nanoparticles for the next generation of nanomedicine, *ACS Nano* 13 (2019) 6178–6206.
- [2] G. Bor, et al., Cell medium-dependent dynamic modulation of size and structural transformations of binary phospholipid/ $\omega$ -3 fatty acid liquid crystalline nano-self-assemblies: implications in interpretation of cell uptake studies, *J. Colloid Interface Sci.* 606 (2022) 464–479.
- [3] N. Tran, et al., Manipulating the ordered nanostructure of self-assembled monoolein and Phytantriol nanoparticles with unsaturated fatty acids, *Langmuir* 34 (2018) 2764–2773.
- [4] C.A. Mirkin, et al., Blueprints for better drugs: the structural revolution in nanomedicine, *ACS Nano* 19 (2025) 18889–18901.
- [5] A. Yaghmur, S.M. Moghimi, Intrinsic and dynamic heterogeneity of nonlamellar lyotropic liquid crystalline Nanodispersions, *ACS Nano* 17 (2023) 22183–22195.
- [6] R. Tenchov, R. Bird, A.E. Curtze, Q. Zhou, Lipid nanoparticles—from liposomes to mRNA vaccine delivery, a landscape of research diversity and advancement, *ACS Nano* 15 (2021) 16982–17015.
- [7] G. Bor, et al., PEGylation of phosphatidylglycerol/docosahexaenoic acid Hexosomes with D- $\alpha$ -Tocopheryl succinate poly(ethylene glycol) 2000 induces morphological transformation into vesicles with prolonged circulation times, *ACS Appl. Mater. Interfaces* 14 (2022) 48449–48463.
- [8] M. Fornasier, S. Murgia, Non-lamellar lipid liquid crystalline nanoparticles: a smart platform for nanomedicine applications, *Front. Soft. Matter* 3 (2023) 1109508.
- [9] A. Yaghmur, S. Ghayas, H. Jan, G.D. Kalaycioglu, S.M. Moghimi, Omega-3 fatty acid nanocarriers: characterization and potential applications, *Curr. Opin. Colloid Interface Sci.* 67 (2023) 101728.
- [10] M.A.S. Abourehab, et al., Cubosomes as an emerging platform for drug delivery: a review of the state of the art, *J. Mater. Chem. B* 10 (2022) 2781–2819.
- [11] A. Yaghmur, H. Mu, Recent advances in drug delivery applications of cubosomes, hexosomes, and solid lipid nanoparticles, *Acta Pharm. Sin.* B 11 (2021) 871–885.
- [12] C.A. Mirkin, M. Mrksich, N. Artzi, The emerging era of structural nanomedicine, *Nat Rev Bioeng* (2025), <https://doi.org/10.1038/s44222-025-00306-5>.
- [13] H. Yu, et al., Inverse cubic and hexagonal mesophase evolution within ionizable lipid nanoparticles correlates with mRNA transfection in macrophages, *J. Am. Chem. Soc.* jacs.3c08729 (2023), <https://doi.org/10.1021/jacs.3c08729>.
- [14] X. Xu, T. Xia, Recent advances in site-specific lipid nanoparticles for mRNA delivery, *ACS Nanosci. Au* 3 (2023) 192–203.
- [15] J. Iscaro, et al., Lyotropic liquid crystalline phase nanostructure and cholesterol enhance lipid nanoparticle mediated mRNA transfection in macrophages, *Adv. Funct. Mater.* 34 (2024) 2405286.
- [16] M. Massaro, et al., Lipid nanoparticle-mediated mRNA delivery in lung fibrosis, *Eur. J. Pharm. Sci.* 183 (2023) 106370.
- [17] E. Blanco, H. Shen, M. Ferrari, Principles of nanoparticle design for overcoming biological barriers to drug delivery, *Nat. Biotechnol.* 33 (2015) 941–951.
- [18] M. Masserini, Nanoparticles for brain drug delivery, *ISRN Biochemistry* 2013 (2013) 1–18.
- [19] N. Aliakbarinadehi, et al., Time-resolved inspection of ionizable lipid-facilitated lipid nanoparticle disintegration and cargo release at an early endosomal membrane mimic, *ACS Nano* 18 (2024) 22989–23000.
- [20] Z. Li, et al., Acidification-induced structure evolution of lipid nanoparticles correlates with their *in vitro* gene transfections, *ACS Nano* 17 (2023) 979–990.
- [21] K. Hashiba, et al., Impact of lipid tail length on the organ selectivity of mRNA-lipid nanoparticles, *Nano Lett.* acs.nanolett.4c02566 (2024), <https://doi.org/10.1021/acs.nanolett.4c02566>.



- [22] H. Yu, et al., pH-dependent lyotropic liquid crystalline mesophase and ionization behavior of Phytantriol-based ionizable lipid nanoparticles, *Small* 20 (2024) 2309200.
- [23] Y.H. Park, et al., Omega-3 fatty acid-type docosahexaenoic acid protects against  $\alpha$ -mediated mitochondrial deficits and Pathomechanisms in Alzheimer's disease-related animal model, *IJMS* 21 (2020) 3879.
- [24] M.E. Surette, Dietary omega-3 PUFA and health: Stearidonic acid-containing seed oils as effective and sustainable alternatives to traditional marine oils, *Mol. Nutr. Food Res.* 57 (2013) 748–759.
- [25] C. Kousparou, M. Fyrrilla, A. Stephanou, I. Patrikios, DHA/EPA (Omega-3) and LA/GLA (Omega-6) as bioactive molecules in neurodegenerative diseases, *IJMS* 24 (2023) 10717.
- [26] I. Djuricic, P.C. Calder, Beneficial outcomes of Omega-6 and Omega-3 polyunsaturated fatty acids on human health: an update for 2021, *Nutrients* 13 (2021) 2421.
- [27] P.C. Calder, Omega-3 fatty acids and inflammatory processes: from molecules to man, *Biochem. Soc. Trans.* 45 (2017) 1105–1115.
- [28] K. Mayurasakorn, et al., DHA but not EPA emulsions preserve neurological and mitochondrial function after brain hypoxia-ischemia in neonatal mice, *PLoS One* 11 (2016) e0160870.
- [29] M.C. Morris, D.A. Evans, C.C. Tangney, J.L. Bienias, R.S. Wilson, Fish consumption and cognitive decline with age in a large community study, *Arch. Neurol.* 62 (2005) 1849.
- [30] B. Xiao, et al., Eicosapentaenoic acid (EPA) exhibits antioxidant activity via mitochondrial modulation, *Food Chem.* 373 (2022) 131389.
- [31] T. Akanchise, A. Ginkgo Angelova, Biloba and Long COVID: In vivo and in vitro models for the evaluation of nanotherapeutic efficacy, *Pharmaceutics* 15 (2023) 1562.
- [32] G. Derosa, P. Maffioli, A. D'Angelo, F. Di Pierro, A role for quercetin in coronavirus disease 2019 (COVID-19), *Phytother. Res.* 35 (2021) 1230–1236.
- [33] M. Gachowska, W. Szlasa, J. Saczko, J. Kulbacka, Neuroregulatory role of ginkgolides, *Mol. Biol. Rep.* 48 (2021) 5689–5697.
- [34] Y. Wu, et al., Sustained CREB phosphorylation by lipid-peptide liquid crystalline nanoassemblies, *Commun Chem* 6 (2023) 241.
- [35] K. Debnath, N.R. Jana, N.R. Jana, Quercetin encapsulated polymer nanoparticle for inhibiting intracellular polyglutamine aggregation, *ACS Appl. Bio Mater.* 2 (2019) 5298–5305.
- [36] S. Rajesh, J. Zhai, C.J. Drummond, N. Tran, Synthetic ionizable aminolipids induce a pH dependent inverse hexagonal to bicontinuous cubic lyotropic liquid crystalline phase transition in monoolein nanoparticles, *J. Colloid Interface Sci.* 589 (2021) 85–95.
- [37] N. Kongkatigumjorn, et al., Controlling endosomal escape using pH-responsive nanoparticles with Tunable disassembly, *ACS Appl. Nano Mater.* 1 (2018) 3164–3173.
- [38] R. Prajapati, M. Gontsarik, A. Yaghmur, S. Salentinig, pH-responsive Nano-self-assemblies of the anticancer drug 2-Hydroxyoleic acid, *Langmuir* 35 (2019) 7954–7961.
- [39] S. Salentinig, L. Sagalowicz, O. Glatter, Self-assembled structures and p  $K_a$  value of oleic acid in Systems of Biological Relevance, *Langmuir* 26 (2010) 11670–11679.
- [40] J. Kurniawan, K. Suga, T.L. Kuhl, Interaction forces and membrane charge tunability: oleic acid containing membranes in different pH conditions, *Biochimica et Biophysica acta (BBA) - Biomembranes* 1859 (2017) 211–217.
- [41] S. Skulj, M. Vazdar, Calculation of apparent p  $K_a$  values of saturated fatty acids with different lengths in DOPC phospholipid bilayers, *Phys. Chem. Chem. Phys.* 21 (2019) 10052–10060.
- [42] A.W. Boots, M. Drent, V.C.J. de Boer, A. Bast, G.R.M.M. Haenen, Quercetin reduces markers of oxidative stress and inflammation in sarcoidosis, *Clin. Nutr.* 30 (2011) 506–512.
- [43] T. Yoshitake, S. Yoshitake, J. Kehr, The *Ginkgo biloba* extract EGB 761® and its main constituent flavonoids and ginkgolides increase extracellular dopamine levels in the rat prefrontal cortex, *British J Pharmacology* 159 (2010) 659–668.
- [44] A.K. Aranda-Rivera, A. Cruz-Gregorio, Y.L. Arancibia-Hernández, E.Y. Hernández-Cruz, J. Pedraza-Chaverri, RONS and oxidative stress: an overview of basic concepts, *Oxygen* 2 (2022) 437–478.
- [45] D. Yu, et al., Neuroprotective effects of Ginkgo biloba dropping pills in Parkinson's disease, *Journal of Pharmaceutical Analysis* 11 (2021) 220–231.
- [46] Y.-Q. Wang, et al., Neuroprotective effects of ginkgetin against neuroinjury in Parkinson's disease model induced by MPTP via chelating iron, *Free Radic. Res.* 49 (2015) 1069–1080.
- [47] V. Rhein, et al., Ginkgo biloba extract ameliorates oxidative phosphorylation performance and rescues  $\alpha$ -induced failure, *PLoS One* 5 (2010) e12359.
- [48] H.M. Mahdy, M.G. Tadros, M.R. Mohamed, A.M. Karim, A.E. Khalifa, The effect of Ginkgo biloba extract on 3-nitropropionic acid-induced neurotoxicity in rats, *Neurochem. Int.* 59 (2011) 770–778.
- [49] M. Jiang, et al., Neuroprotective effects of bilobalide on cerebral ischemia and reperfusion injury are associated with inhibition of pro-inflammatory mediator production and down-regulation of JNK1/2 and p38 MAPK activation, *J. Neuroinflammation* 11 (2014) 167.
- [50] W. Li, et al., The protective role of isorhamnetin on human brain microvascular endothelial cells from cytotoxicity induced by methylglyoxal and oxygen-glucose deprivation, *J. Neurochem.* 136 (2016) 651–659.
- [51] L. Wang, et al., Ginkgolide B maintains calcium homeostasis in hypoxic hippocampal neurons by inhibiting calcium influx and intracellular calcium release, *Front. Cell. Neurosci.* 14 (2021) 627846.
- [52] F. Tchantchou, Y. Xu, Y. Wu, Y. Christen, Y. Luo, EGB 761 enhances adult hippocampal neurogenesis and phosphorylation of CREB in transgenic mouse model of Alzheimer's disease, *FASEB J.* 21 (2007) 2400–2408.
- [53] F. Ciscato, et al., Hexokinase 2 displacement from mitochondria-associated membranes prompts  $Ca^{2+}$ -dependent death of cancer cells, *EMBO Rep.* 21 (2020) e49117.
- [54] O. Vergun, I.J. Reynolds, Fluctuations in mitochondrial membrane potential in single isolated brain mitochondria: modulation by adenine nucleotides and  $Ca^{2+}$ , *Biophys. J.* 87 (2004) 3585–3593.
- [55] L.D. Zorova, et al., Mitochondrial membrane potential, *Anal. Biochem.* 552 (2018) 50–59.
- [56] T. Akanchise, B. Angelov, A. Angelova, Nanomedicine-mediated recovery of antioxidant glutathione peroxidase activity after oxidative-stress cellular damage: insights for neurological long COVID, *J. Med. Virol.* 96 (2024) e29680.
- [57] M. Rakotoarisoa, et al., Composition-switchable liquid crystalline nanostructures as green formulations of curcumin and fish oil, *ACS Sustain. Chem. Eng.* 9 (2021) 14821–14835.
- [58] T. Akanchise, et al., Nanostructuring and antioxidant activity of nanotherapeutics designed by self-assembly of natural lipids and phytochemicals, *ACS Biomater. Sci. Eng.* acsbiomaterials.5c00006 (2025), <https://doi.org/10.1021/acsbomaterials.5c00006>.
- [59] H. Yu, et al., Real-time pH-dependent self-assembly of ionisable lipids from COVID-19 vaccines and *in situ* nucleic acid complexation, *Angew. Chem.* 135 (2023) e202304977.
- [60] B. Angelov, et al., Multicompartment lipid cubic nanoparticles with high protein upload: millisecond dynamics of formation, *ACS Nano* 8 (2014) 5216–5226.
- [61] A. Mortazavi, B.A. Williams, K. McCue, L. Schaeffer, B. Wold, Mapping and quantifying mammalian transcriptomes by RNA-Seq, *Nat. Methods* 5 (2008) 621–628.
- [62] Z. Wang, M. Gerstein, M. Snyder, RNA-Seq: a revolutionary tool for transcriptomics, *Nat. Rev. Genet.* 10 (2009) 57–63.
- [63] M. Pertea, et al., StringTie enables improved reconstruction of a transcriptome from RNA-seq reads, *Nat. Biotechnol.* 33 (2015) 290–295.
- [64] M.I. Love, W. Huber, S. Anders, Moderated estimation of fold change and dispersion for RNA-seq data with DESeq2, *Genome Biol.* 15 (2014).
- [65] Y. Liao, G.K. Smyth, W. Shi, featureCounts: an efficient general purpose program for assigning sequence reads to genomic features, *Bioinformatics* 30 (2014) 923–930.
- [66] M.D. Young, M.J. Wakefield, G.K. Smyth, A. Oshlack, Gene ontology analysis for RNA-seq: accounting for selection bias, *Genome Biol.* 11 (2010).
- [67] Z. He, et al., Comparative transcriptome and gene co-expression network analysis reveal genes and signaling pathways adaptively responsive to varied adverse stresses in the insect fungal pathogen, *Beauveria bassiana*, *J. Invertebr. Pathol.* 151 (2018) 169–181.
- [68] A. McKenna, et al., The genome analysis toolkit: a MapReduce framework for analyzing next-generation DNA sequencing data, *Genome Res.* 20 (2010) 1297–1303.
- [69] S. Shen, et al., rMATS: robust and flexible detection of differential alternative splicing from replicate RNA-Seq data, *Proc. Natl. Acad. Sci. USA* 111 (2014).